RAA 2021 Vol. **21** No. **5**, 123(16pp) doi: 10.1088/1674-4527/21/5/123

http://www.raa-journal.org *http://iopscience.iop.org/raa*

***R**esearch in*
***A**stronomy and*
***A**strophysics*

The HI gas and star formation in star-forming galaxies selected from ALFALFA

Feng-Jie Lei (雷凤杰)[1,3], Hong Wu (吴宏)[1,2,3], Yi-Nan Zhu (朱轶楠)[4], Man I. Lam (林敏仪)[3] and Zhi-Min Zhou (周志民)[1,3]

[1] CAS Key Laboratory of Optical Astronomy, National Astronomical Observatories, Chinese Academy of Sciences, Beijing 100101, China; *fjlei@nao.cas.cn*
[2] School of Astronomy and Space Science, University of Chinese Academy of Sciences, Beijing 100049, China; *hwu@bao.ac.cn*
[3] National Astronomical Observatories, Chinese Academy of Sciences, Beijing 100101, China
[4] Schools of Physics and Astronomy, Sun Yat-sen University, Zhuhai 519082, China

Received 2020 November 9; accepted 2020 December 22

Abstract This paper presents the results of Hα imaging of 169 galaxies randomly selected from the α.40 - SDSS catalog. The sample has excluded all low surface brightness galaxies (LSBGs) whose central surface brightness in B band (μ_0(B)) fainter than 22.5 $\mathrm{mag\ arcsec^{-2}}$. It can be used as the counterparts sample to LSBGs. We observed their Hα and R band images by using the 2.16 m telescope at the Xinglong Observatory of the National Astronomical Observatories, Chinese Academy of Sciences (NAOC). The main goal of this work is to present the properties of those galaxies, together with Hα flux and star formation-, gas-, stellar mass- surface density. In addition, we confirm the correlations among HI content, stellar mass and star formation in ALFALFA galaxies. The HI mass increases with stellar mass, and the slope slows down at the higher stellar mass. The overall trend was that the specific star formation rate (sSFR) decreases with stellar mass, and the sSFR dropped sharply when the stellar mass is close to $10^{10.3} \sim 10^{10.5} M_{\odot}$. The weak correlation between $\mathrm{SFR/M_{HI}}$ and M_{HI} implies the HI contribute little to star formation. Our sample, which are mostly star-forming galaxies, follows the revisited Kennicutt-Schmidt law as well as the Kennicutt-Schmidt law.

Key words: techniques: image processing — galaxies: star formation — catalogs

1 INTRODUCTION

To understand the physics of evolution and formation in galaxies, it is crucial to know the star formation rate (SFR). Young and massive stars have relatively short lifetime, thus their presentation traces recent star formation (SF) in galaxies. Many star formation tracers including emission-lines (Hα, Hβ $\cdots$), UV, IR, radio luminosity relate to new formed stars. Among those star formation traces, the most commonly used is Hα which indicates young ($<$ 10 Myr), massive ($>$ 17 $M_{\odot}$), short-lived OB stars and is easier to be observed because it emits relatively strong line (Kennicutt & Evans 2012; Watson et al. 2016). Hα emission can be obtained by spectroscopic mode or by imaging mode. Hα imaging is superior to Hα spectrum in obtaining the fluxes of the whole galaxy.

To achieve a more complete picture of the galaxies, many works have combined observations of Hα and HI survey. The ALFALFA, a successful blind HI survey, covers 7000 $\mathrm{deg^2}$ of sky (Haynes et al. 2011). Recent Hα imaging surveys of ALFALFA, ALFALFA Hα survey(Van Sistine et al. 2016) and Hα3 (Gavazzi et al. 2012, 2013a,b; Fossati et al. 2013; Gavazzi et al. 2015a,b), provide an opportunity to study the relations between HI gas and star formation. The ALFALFA Hα survey contains 1555 galaxies. The Hα3 survey is an Hα imaging survey of galaxies in Virgo and Coma cluster selected from ALFALFA. In addition, Lei et al. (2018, 2019) presented the results of Hα imaging observations for 468 low surface brightness galaxies (LSBGs) selected from ALFALFA. Following the LSBGs Hα survey, we also built another Hα survey which only contain high surface brightness galaxies selected from ALFALFA. The sample can be used as the

counterpart to LSBGs to explore the differences in process of converting HI content to star formation.

As HI gas is the raw fuel for molecular clouds and stars, it is worth studying the relationships of HI content with galaxy properties, such as SFR, stellar mass$\cdots$. In comparison to the relation between hydrogen molecular gas (M_{H_2}) and SFR, the link between M_{HI} and SFR is less straightforward (Krumholz 2012; Jaskot et al. 2015). Low-mass galaxies tend to be more HI rich (Gavazzi et al. 1996; Huang et al. 2012b; Jaskot et al. 2015). M_{HI}/M_* correlates weakly with sSFR as well as color (Jaskot et al. 2016).

The relationship between gas and star formation has been well studied in many previous works. It should be noted the correlation between the HI surface density (Σ_{HI}) and SFR surface density (Σ_{SFR}). Bigiel et al. (2008) found there is no or little correlation between Σ_{HI} and Σ_{SFR} in a sub-kpc scale. Lei et al. (2019) examined 468 LSBGs as well as star-forming galaxies from Kennicutt (1998) in a global scale and then found there was little correlation between Σ_{HI} and Σ_{SFR} which is consistent with the previous results in Bigiel et al. (2008). The Σ_{HI} of all galaxies are in the range 0.2–1.5$M_\odot pc^{-2}$. However the Σ_{SFR} of star-forming galaxies are higher than those of LSBGs. Base on the above results, HI alone is insufficient to predict SF well.

The relation between gas surface density (Σ_{gas}, a combination of molecular gas and neutral gas) and SFR surface density (Σ_{SFR}) can be described by an empirical law. Kennicutt (1998) have posed a power-law relation ($\Sigma_{SFR} \propto \Sigma_{gas}^{1.4}$), known as Kennicutt-Schmidt (K-S) law. de los Reyes & Kennicutt (2019) revise K-S law with the sample of the local quiescent spiral, dwarf, and LSBGs without starburst galaxies by updated gas and star formation surface density. However the star formation is a complex process, the gas dependence alone cannot be a full story. The gas and star formation relation are not held for all types of galaxies, there is turnover in the low gas density region. Shi et al. (2011, 2014, 2018) emphasize the star formation also affect by the existing stars. The relation is $\Sigma_{SFR} \propto \Sigma_{gas}^{n}\Sigma_{star}^{m}$, where Σ_{star} is the stellar mass surface density, n and m are different power law indices. It also holds for the low Σ_{gas} galaxies and faint regions in the outer part of the galaxy.

From 2013–2018, we have undertaken a project measuring the SFR of LSBGs and normal galaxies in ALFALFA by using Hα observations. We have finished 468 LSBG targets (Lei et al. 2018, 2019). Following up the LSBG sample, this work contains randomly selected 169 galaxies from the rest of the non-LSBGs in α.40-SDSS catalog. In this paper, we aim to present the results of Hα imaging of 169 galaxies and study the process that galaxies' abilities consume their HI gas and form new stars. The layout of this article is as follows: in Section 2, we introduce our sample together with a description of the observations and the data reduction. In Section 3, we present the catalog of Hα flux and some derived parameters. The major results are presented in Sections 4 and 5. Summary is shown in Section 6. Throughout the paper we adopt a flat ΛCDM cosmology, with H_0 = 70 km $s^{-1}Mpc^{-1}$ and Ω_Λ = 0.7, and a Salpeter Initial Mass Function (IMF) $[dN(m)/dm = -2.35]$ over $m = 0.1 - 100M_\odot$ (Salpeter 1955).

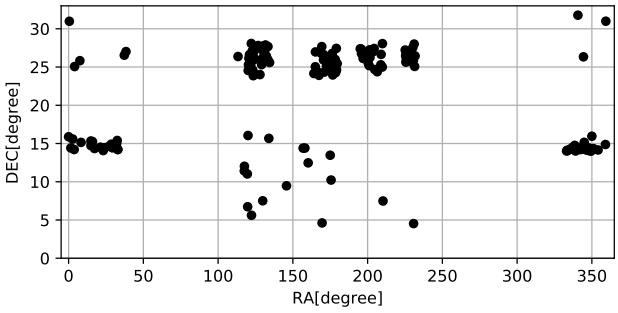

Fig. 1 The sky distribution of the 169 galaxies selected from the α.40.

2 SAMPLE AND OBSERVATIONS

2.1 Sample and α.40 Catalog

The Arecibo Legacy Fast ALFA (ALFALFA) survey (Giovanelli et al. 2005a,b) is a blind extragalactic HI survey, mapping about 7000 deg^2, with an L-band (1.4 GHz) receiver in Arecibo radio telescope. It has detected more than 30 000 extragalactic sources, providing an HI line spectral database out to $z \sim 0.06$ and HI masses greater than $10^6M_\odot$. α.40 catalog (Haynes et al. 2011) containing HI 15 855 sources and covering 40% of ALFALFA survey area, is the first version of the released data. α.40 catalog also provides a cross-reference of sources with the SDSS DR7 photometric database.

Du et al. (2015) selected 1129 non-edge-on LSBGs ($\mu_0(B) > 22.5$ mag arcsec^{-2}) from the α.40 and SDSS, hereafter Du2015. Lei et al. (2018, 2019) present the results of Hα images 468 LSBGs which belong to Du2015. In this paper, we want to build an Hα image sample which is also selected in α.40-SDSS catalog excluding the LSBGs. Limited by observation time, we finished 169 galaxies, and the spatial distribution of them is shown in Figure 1.

Figure 2 shows the histograms of the distance, M_*, M_{HI} and $g - r$ properties of the galaxies in the above four samples. The red dash-dotted line presents the LSBGs sample (Du2015). While the orange dotted line is part of Du2015 with Hα observation (Lei et al. 2018, 2019). The blue dashed line identifies the galaxy sample from cross-

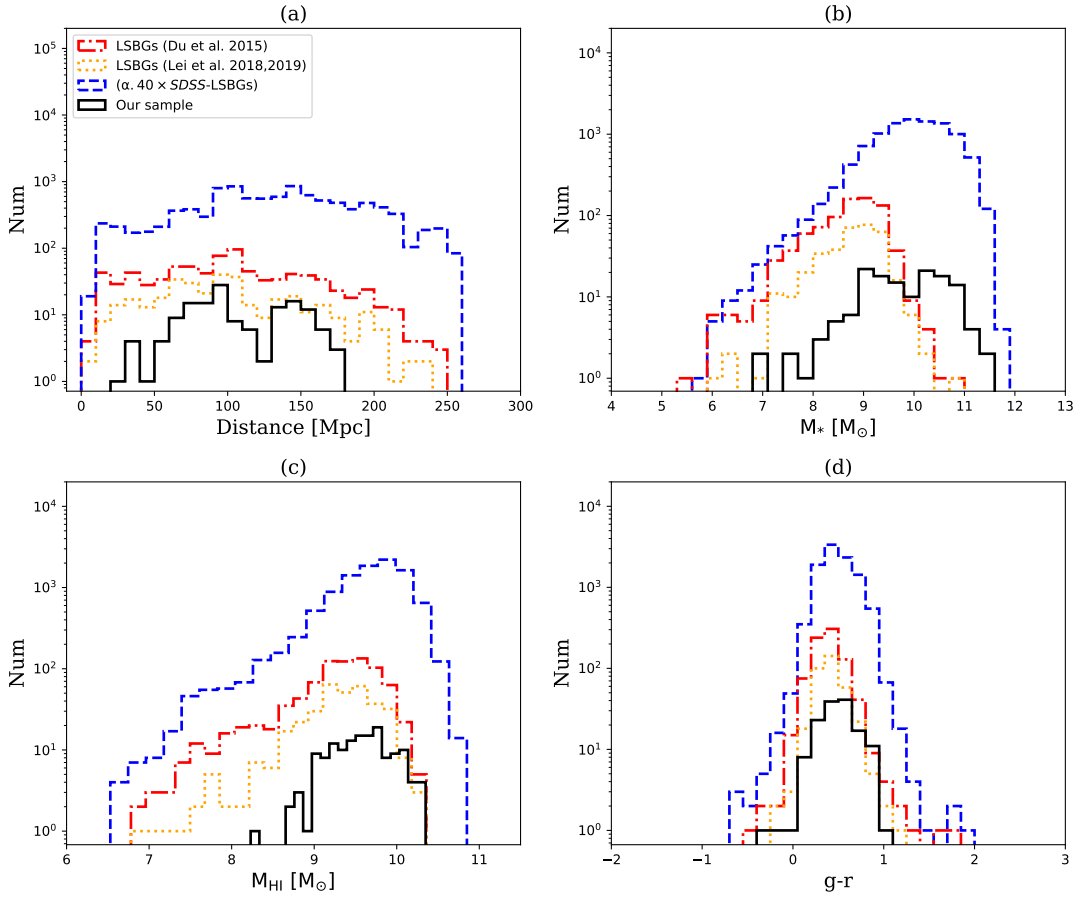

Fig. 2 The distribution of distance, stellar mass, HI mass and $g-r$ color of galaxies in four samples. In all panels, The red dash-dot line shows 1129 LSBGs selected from $\alpha.40$-SDSS. As a part of the above LSBGs sample, the 468/1129 LSBGs with Hα images are shown in orange dotted line. The blue dashed line identifies the galaxies in $\alpha.40$-SDSS sample except for 1129 LSBGs. The black solid line presents the parts of above sample having Hα observation which contains 169 galaxies.

matching between the $\alpha.40$ and SDSS DR7 except for LSBGs (Du2015). It is as our parent sample. Our sample shown in the black line is randomly selected from parent sample with Hα observation.

By comparing with parent sample (blue dashed line), our sample (black line) tends to have lower distance, higher stellar mass, higher HI mass. Compared to LSBG sample (Du2015, red dash-dotted line), our sample is more local and has a median distance of 95.4 Mpc, has a relatively larger stellar mass. Of the total galaxies of Du2015, 54% are dwarf galaxies (Du et al. 2019), so low stellar mass of Du2015 is in large fractions. The color of our sample and LSBGs (Du2015) are both blue. The LSBGs with a median $g-r$ color of 0.31 is bluer than that of 0.44 in our sample which is consistent with the previous results that LSBGs are bluer than normal late-type galaxies (McGaugh 1994).

2.2 Observation

All Hα observations for our sample were finished in 2013 under the photometric conditions. Our observing utilized the BAO Faint Object Spectrograph and Camera instrument (BFOSC) attached to the 2.16-m telescope (Fan et al. 2016) located at Xinglong Observatory of the National Astronomical Observatories, Chinese Academy of Sciences (NAOC). This instrument is a R-C system with the focal ratio f/9 Cassegrain focus. The size of the charge coupled device (CCD) detector is 1242×1152 pixel^2 with the pixel scale of $0''.457$ pixel^{-1}, giving a total field of view of over 9.5×8.5 arcmin^2. The detector was used in the 1.08 e^{-1} ADU^{-1} gain mode.

The observing data contains Hα-band images and auxiliary (R-band, bias and flat) images. Hα-band filters are designed to obtain Hα emission (rest-frame wavelength of λ 6563 Å) of galaxies, there are 11 Hα filters which can cover the redshift up to 0.074 with the full width at half

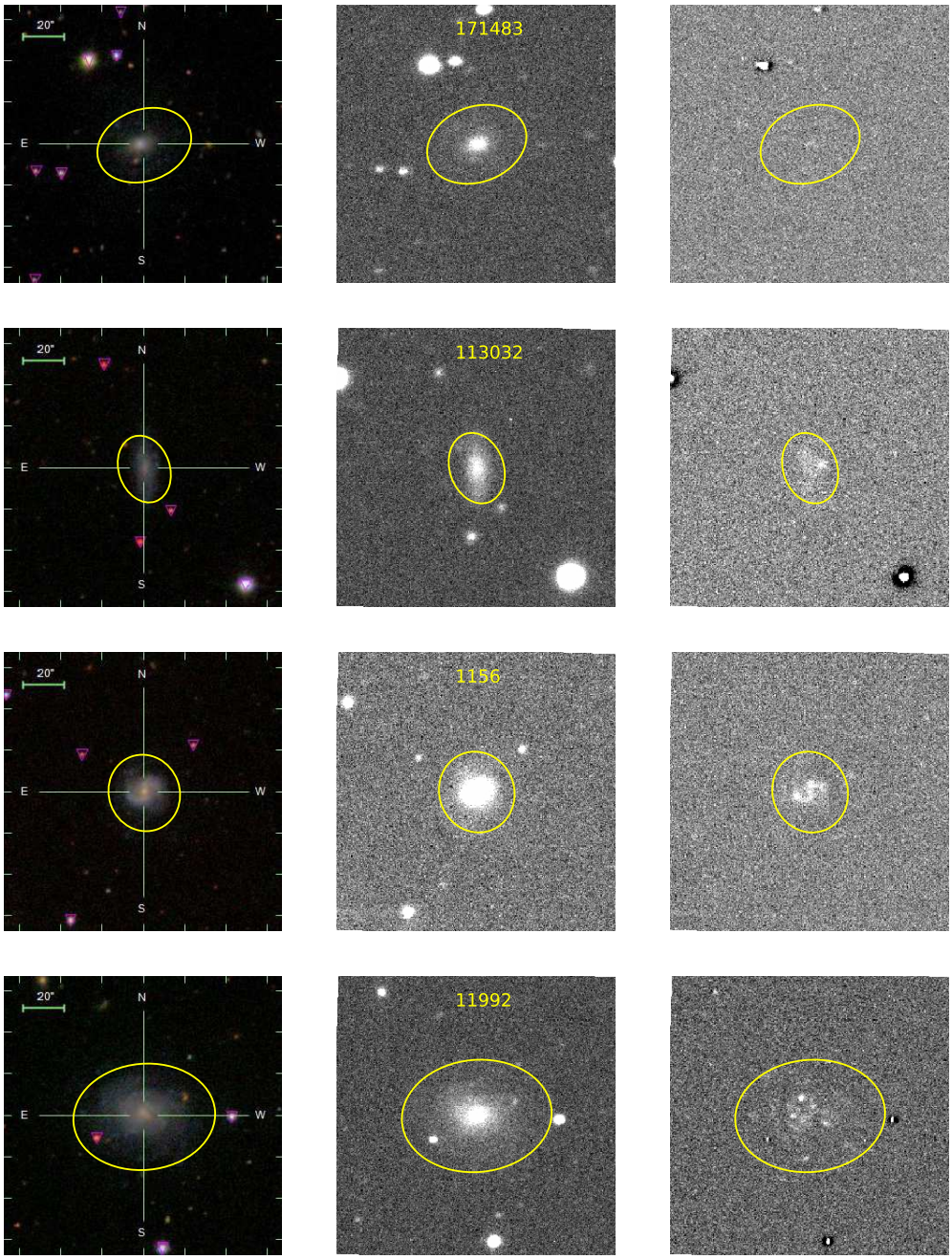

Fig. 3 Example of four galaxies of our sample after data reduction. The left, middle and right panels show the galaxy in SDSSS color, R and continuum-subtracted images, respectively. The yellow ellipse shows the photometric aperture which reach to 25 $\mathrm{magarcsec}^2$.

maximum (FWHM) about 55 Å. The transmission of the Hα filters can be referred to Lei et al. (2018). The R-band images are used to continuum subtraction as well as flux calibration. The effective wavelength $\lambda_{\rm eff}$ of the R band filter is 6407 Å with the FWHM about 1200 Å. For each galaxy, the R band and Hα band images were observed with the integration time of 300 s and 1500 s, respectively. The observatory information is listed in Table 1.

2.3 Data Reduction

All images were performed in the following orders: overscan correction, bias subtraction, image trimming, flat-field correction, cosmic rays removal, world coordinate system (WCS) calibration, background subtraction, continuum subtraction, photometry, flux correction, and flux calibration. Readers are referred to Lei et al. (2018, 2019) for details of the data reduction.

Table 1 Observed Information and Main Parameters of Our Sources

AGCN	ra J2000	dec J2000	z	Distance Mpc	g	r	W3	type	Filter	Date
(1)	(2)	(3)	(4)	(5)	(6)	(7)	(8)	(9)	(10)	(11)
43	00:06:02	14:25:01	0.0176	74.8	16.81	16.29	···	S	Ha3	20131005
615	00:59:40	15:19:50	0.0183	76.8	14.36	13.58	7.89	A	Ha3	20131005
619	00:59:48	14:43:24	0.0407	169.8	16.63	15.83	9.15	S	Ha6	20131005
717	01:09:22	14:20:31	0.0384	160.2	14.30	13.50	9.98	A	Ha6	20131006
985	01:25:23	14:31:10	0.0370	154.0	14.73	13.86	8.78	A	Ha6	20131008
1156	01:37:20	14:27:46	0.0353	147.1	16.00	15.48	10.39	S	Ha6	20131008
1364	01:54:03	14:54:33	0.0170	70.4	22.92	21.76	11.75	S	Ha3	20131010
1556	02:03:49	14:44:21	0.0122	49.6	13.80	12.79	9.11	C	Ha3	20131005
1589	02:05:58	14:55:09	0.0416	174.4	15.18	14.40	9.01	unknown	Ha7	20131005
1630	02:08:24	14:58:18	0.0148	60.8	14.11	13.52	7.12	unknown	Ha3	20131006
4167	08:01:18	25:17:21	0.0151	66.1	16.12	15.82	11.98	unknown	Ha3	20131229
4210	08:05:05	25:03:43	0.0167	72.8	15.46	14.83	8.77	S	Ha3	20130210
4275	08:12:46	26:21:39	0.0209	93.1	14.16	13.52	7.58	S	Ha4	20130213
4456	08:32:03	24:00:37	0.0183	79.8	13.80	13.40	9.66	S	Ha3	20130412
4509	08:38:23	25:45:15	0.0185	80.5	14.34	13.66	5.59	unknown	Ha3	20130410
4570	08:45:16	27:49:22	0.0215	95.4	16.78	15.78	11.01	unknown	Ha4	20130411
4597	08:47:40	25:53:35	0.0218	97.0	14.86	14.32	7.69	unknown	Ha4	20130411
4602	08:47:55	25:49:51	0.0189	82.3	14.61	13.87	9.81	C	Ha4	20130409
5189	09:42:58	09:28:15	0.0107	48.9	20.84	20.90	···	unknown	Ha2	20131230
5812	10:40:56	12:28:18	0.0034	11.1	22.68	22.06	···	unknown	Ha2	20131230
6204	11:09:51	24:15:41	0.0202	90.9	14.47	13.96	7.14	S	Ha4	20130410
6302	11:17:21	27:40:20	0.0194	87.5	15.44	14.67	7.87	S	Ha4	20130409
6317	11:18:08	04:36:57	0.0077	35.6	15.80	15.49	···	S	Ha2	20131230
6627	11:39:55	13:28:01	0.0118	53.2	15.99	15.57	···	S	Ha3	20131231
6751	11:46:42	23:57:47	0.0213	95.8	18.76	18.09	9.57	S	Ha4	20130412
6795	11:49:21	24:56:17	0.0199	89.6	15.11	14.69	9.91	S	Ha4	20130409
8911	13:59:39	28:03:38	0.0365	159.5	15.36	14.85	9.63	C	Ha6	20130411
8927	14:01:10	07:28:54	0.0237	105.2	15.39	14.90	10.51	unknown	Ha4	20140331
9679	15:03:45	26:06:01	0.0311	135.7	14.99	14.07	9.04	unknown	Ha5	20130410
9830	15:23:00	04:31:45	0.0061	29.3	22.06	24.80	11.16	unknown	Ha2	20140401
11948	22:12:22	14:01:27	0.0265	108.6	14.91	14.06	7.74	unknown	Ha5	20131005
11992	22:20:47	14:14:03	0.0120	53.4	15.61	15.08	10.52	S	Ha3	20131006
12270	22:58:10	14:18:29	0.0070	31.4	13.46	12.90	10.29	C	Ha2	20131006
12481	23:17:36	14:00:02	0.0147	63.4	15.23	14.80	6.56	unknown	Ha3	20131005
12519	23:20:02	15:57:09	0.0146	62.9	14.19	13.51	8.06	unknown	Ha3	20131006
12705	23:36:37	14:09:25	0.0132	56.6	15.78	15.16	10.91	S	Ha3	20131005
12864	23:57:24	30:59:31	0.0156	66.4	14.59	13.77	8.47	unknown	Ha3	20131231
101934	00:10:52	15:35:26	0.0367	152.3	16.30	15.26	10.23	lowSNR	Ha6	20131006
102634	00:16:00	25:03:43	0.0358	148.6	17.51	17.18	···	unknown	Ha6	20130102
102654	00:30:08	25:49:47	0.0330	136.9	17.97	17.80	···	unknown	Ha5	20130101
102735	00:02:01	30:58:58	0.0096	40.6	18.36	18.29	···	unknown	Ha2	20131230
112457	01:59:26	14:50:02	0.0070	28.1	15.72	15.21	12.04	S	Ha2	20131006
113032	01:32:39	14:04:50	0.0229	93.7	17.04	16.56	···	S	Ha4	20131010
113209	01:57:05	14:26:03	0.0269	111.5	17.05	16.69	10.95	S	Ha5	20131005
113800	01:03:58	15:14:49	0.0417	174.1	15.93	15.13	8.22	S	Ha7	20131005
121273	02:10:03	15:23:48	0.0132	54.1	18.17	17.29	9.84	unknown	Ha3	20131006
122141	02:11:33	14:14:18	0.0127	51.7	17.86	18.23	11.38	unknown	Ha3	20131010
122217	02:33:32	27:01:14	0.0055	22.1	21.58	20.04	···	unknown	Ha2	20131230
122265	02:02:49	14:31:14	0.0321	133.6	16.23	15.94	9.81	S	Ha5	20131008
122405	02:11:31	14:12:02	0.0254	105.1	15.85	15.05	···	A	Ha4	20131006
122806	02:28:59	26:32:40	0.0317	132.4	24.56	23.04	···	unknown	Ha5	20130101
171483	07:58:12	11:01:14	0.0078	35.8	16.48	16.14	···	S	Ha2	20131230
172836	07:59:59	16:03:01	0.0151	66.7	17.73	17.22	11.54	lowSNR	Ha3	20131231
174511	07:50:23	12:01:31	0.0294	129.1	17.90	17.57	···	unknown	Ha5	20131228
174604	07:50:02	11:25:24	0.0325	142.5	17.94	17.75	···	unknown	Ha5	20131228
174653	07:33:20	26:22:26	0.0077	34.1	21.52	20.90	···	unknown	Ha2	20131230
174720	07:59:06	06:44:02	0.0086	39.7	22.32	21.97	···	unknown	Ha2	20131230
180049	08:07:27	25:08:02	0.0207	91.6	14.54	13.95	7.14	S	Ha4	20130213
180111	08:13:03	24:34:01	0.0204	90.7	16.70	16.06	9.15	S	Ha4	20130212
180612	08:14:06	23:51:57	0.0204	90.4	14.30	13.54	6.71	unknown	Ha4	20130212
180649	08:36:47	27:19:58	0.0204	90.7	15.79	15.39	10.39	unknown	Ha4	20130212
180659	08:47:06	27:52:23	0.0207	91.6	15.56	15.02	10.21	S	Ha4	20130213
180939	08:08:46	28:04:44	0.0187	81.0	16.06	15.67	11.95	S	Ha4	20130210
181122	08:43:06	26:48:19	0.0172	75.1	15.22	14.63	8.30	S	Ha3	20130410
181143	08:46:15	27:20:39	0.0188	81.8	16.53	16.15	9.69	unknown	Ha4	20130412
181774	08:39:21	07:30:33	0.0300	132.7	17.49	17.28	···	S	Ha5	20131228
181925	08:09:21	05:36:56	0.0274	121.1	17.34	17.02	12.08	S	Ha5	20131228
182630	08:00:28	24:33:10	0.0156	68.1	23.00	23.24	···	S	Ha3	20131229

Table 1 *Continued.*

AGCN	ra J2000	dec J2000	z	Distance Mpc	g	r	W3	type	Filter	Date
(1)	(2)	(3)	(4)	(5)	(6)	(7)	(8)	(9)	(10)	(11)
182736	08:02:42	26:10:14	0.0272	119.7	21.31	21.85	···	S	Ha5	20130214
182762	08:03:13	26:05:23	0.0267	117.2	18.07	17.75	···	S	Ha5	20130214
182798	08:03:52	26:36:52	0.0204	90.1	16.72	16.27	···	S	Ha4	20130212
182858	08:05:22	25:27:25	0.0170	73.8	17.96	17.69	···	S	Ha3	20130208
182859	08:05:22	25:32:30	0.0172	74.7	16.53	16.25	···	S	Ha3	20130210
183012	08:11:02	27:04:35	0.0187	81.1	17.43	17.05	···	S	Ha4	20130210
183074	08:13:49	26:15:17	0.0266	117.2	17.28	16.83	11.37	S	Ha5	20130214
183105	08:14:48	25:55:17	0.0209	92.7	16.85	16.49	11.83	S	Ha4	20130101
183127	08:15:29	26:09:03	0.0211	93.5	15.48	14.91	9.19	S	Ha4	20130213
183135	08:15:40	27:00:29	0.0251	110.7	17.68	17.33	···	S	Ha4	20130101
183419	08:27:08	27:48:37	0.0203	90.1	16.06	15.45	9.53	S	Ha4	20130213
183852	08:37:45	26:05:20	0.0182	79.2	17.21	16.64	···	S	Ha3	20130210
184340	08:49:00	26:27:02	0.0169	74.0	17.82	17.48	···	S	Ha3	20130210
184444	08:53:08	25:58:41	0.0220	98.1	17.66	17.46	···	S	Ha4	20130411
184450	08:53:24	27:40:38	0.0173	75.4	16.60	16.43	10.07	S	Ha3	20130210
184559	08:57:43	25:35:25	0.0196	89.7	17.06	16.69	11.88	S	Ha4	20130213
188784	08:55:45	15:40:26	0.0142	63.1	18.00	17.67	···	unknown	Ha3	20131229
203102	10:27:25	14:23:39	0.0312	138.3	18.87	18.40	···	S	Ha5	20131228
203105	10:32:09	14:24:11	0.0321	142.3	18.02	17.69	···	S	Ha5	20131228
210271	11:22:02	25:55:14	0.0211	94.7	15.30	14.82	10.46	S	Ha4	20130410
210653	11:43:25	25:00:19	0.0206	92.5	15.37	14.94	9.82	S	Ha4	20130412
211188	11:22:53	26:36:18	0.0200	89.9	16.92	16.40	···	S	Ha4	20130213
213028	11:42:15	10:13:22	0.0156	69.0	17.98	17.67	···	S	Ha3	20131229
219344	11:44:33	25:54:07	0.0257	114.7	19.16	19.16	···	unknown	Ha4	20130212
221378	13:00:17	27:23:13	0.0370	162.2	15.86	15.35	9.03	S	Ha6	20130410
230107	13:08:01	26:45:55	0.0341	149.9	15.24	14.62	8.70	S	Ha6	20130409
230274	13:21:34	25:30:57	0.0337	148.1	14.60	13.86	9.61	A	Ha5	20130409
230488	13:37:24	27:25:10	0.0366	160.3	14.51	13.82	8.42	unknown	Ha6	20130412
231669	13:03:16	27:19:56	0.0358	157.2	16.03	15.48	7.59	S	Ha6	20130412
232123	13:59:17	24:59:54	0.0371	162.4	17.50	16.76	10.74	C	Ha6	20130412
234302	13:08:01	26:07:12	0.0358	157.0	15.45	14.91	9.46	C	Ha6	20130412
234624	13:25:22	27:14:57	0.0346	152.1	15.84	15.24	9.07	S	Ha6	20130409
234900	13:34:12	27:00:11	0.0356	156.0	15.89	15.07	10.34	A	Ha6	20130410
250004	15:02:24	25:38:17	0.0328	142.9	15.42	14.81	9.55	C	Ha5	20130412
250348	15:13:24	26:53:54	0.0312	135.6	25.11	21.15	8.81	C	Ha5	20130411
250802	15:25:48	25:04:44	0.0332	144.1	15.36	14.67	9.19	A	Ha5	20130410
254523	15:24:33	28:00:05	0.0316	137.2	23.48	21.61	···	S	Ha5	20130411
320086	22:13:34	14:06:32	0.0242	98.8	15.63	14.98	9.39	S	Ha4	20131005
320265	22:36:25	14:01:26	0.0237	96.5	16.06	15.45	9.39	S	Ha4	20131006
320271	22:36:49	14:23:12	0.0179	78.0	15.35	14.55	11.53	C	Ha3	20131005
320276	22:37:07	14:13:54	0.0379	157.2	16.04	15.10	6.51	S	Ha6	20131008
320488	22:59:26	15:09:06	0.0381	158.2	15.55	14.91	8.01	S	Ha6	20131008
320513	23:01:28	14:36:03	0.0404	167.8	15.63	14.89	8.07	S	Ha6	20131008
320527	22:15:52	14:04:45	0.0254	103.8	16.25	15.54	7.92	S	Ha4	20131006
321072	22:27:35	14:27:57	0.0356	147.3	17.49	16.92	10.47	S	Ha6	20131008
321083	22:34:04	14:45:10	0.0350	144.9	16.87	16.32	10.78	S	Ha6	20131008
321104	22:40:17	14:29:57	0.0213	86.3	16.53	16.08	11.17	S	Ha4	20131006
321130	22:49:09	14:12:29	0.0378	156.9	16.45	15.96	9.45	S	Ha6	20131008
321227	22:57:31	26:20:09	0.0236	96.1	17.07	16.50	···	unknown	Ha4	20130101
321430	22:42:38	31:46:36	0.0223	91.0	17.89	17.17	12.01	unknown	Ha4	20130101
330039	23:05:19	14:10:13	0.0243	98.7	15.46	14.53	8.23	S	Ha4	20131006
331061	00:00:02	15:52:54	0.0200	85.2	15.45	14.91	8.11	S	Ha4	20131006
332140	23:12:50	14:03:48	0.0157	67.7	20.27	19.69	···	unknown	Ha3	20131231
332369	23:02:10	14:42:20	0.0321	132.2	18.15	17.73	···	S	Ha5	20131228
332406	23:05:52	14:09:57	0.0242	98.5	18.33	17.63	···	lowSNR	Ha4	20131010
332461	23:11:20	14:17:22	0.0393	163.0	16.82	16.31	10.83	S	Ha6	20131229
332628	23:24:21	14:19:59	0.0409	170.0	18.01	17.54	···	S	Ha6	20131229
332876	23:56:15	14:52:14	0.0267	109.3	18.35	18.22	···	lowSNR	Ha5	20131228
719327	11:09:51	23:54:53	0.0205	92.3	17.82	17.47	···	S	Ha4	20130409
721315	08:39:41	27:43:32	0.0186	80.8	16.95	16.45	11.66	S	Ha3	20130210
721317	08:40:30	27:37:50	0.0208	92.3	16.49	15.99	···	S	Ha4	20130212
722743	11:00:28	26:58:30	0.0208	93.4	17.53	17.11	11.58	S	Ha4	20130410
723579	11:26:38	26:21:38	0.0211	94.7	17.07	16.77	11.97	S	Ha4	20130410
724012	11:45:33	26:46:59	0.0261	116.0	18.11	17.86	···	S	Ha4	20130212
724143	11:52:02	25:45:03	0.0189	83.3	15.74	15.40	10.76	S	Ha4	20130210
724186	11:54:14	24:15:44	0.0233	104.4	17.84	17.46	···	S	Ha4	20130212
724236	11:56:19	27:26:16	0.0209	93.7	17.94	17.58	···	S	Ha4	20130411
724244	11:56:28	24:39:52	0.0170	74.9	16.12	15.72	11.70	S	Ha3	20130210

Table 1 *Continued.*

AGCN	ra J2000	dec J2000	z	Distance Mpc	g	r	W3	type	Filter	Date
(1)	(2)	(3)	(4)	(5)	(6)	(7)	(8)	(9)	(10)	(11)
724246	11:56:30	24:34:55	0.0173	76.3	17.74	17.27	···	S	Ha3	20130210
725599	13:26:19	26:14:39	0.0341	149.7	16.03	15.64	10.42	S	Ha6	20130411
725919	13:55:24	25:17:36	0.0375	163.8	22.15	21.92	8.87	unknown	Ha6	20130412
725935	13:56:09	26:39:10	0.0336	147.0	17.76	17.40	···	S	Ha5	20130214
727048	15:19:26	25:37:33	0.0300	130.6	16.14	15.56	9.66	S	Ha5	20130411
727085	15:22:34	25:52:19	0.0332	144.2	16.89	16.33	10.57	lowSNR	Ha5	20130410
727112	15:27:00	26:26:59	0.0331	143.8	16.38	15.87	11.19	S	Ha5	20130411
731528	10:56:08	24:09:25	0.0326	144.0	18.12	17.75	···	S	Ha5	20131228
731598	11:16:12	26:46:45	0.0197	89.0	17.35	17.17	···	lowSNR	Ha4	20130213
731690	11:24:17	24:20:34	0.0193	87.0	16.36	15.99	11.48	S	Ha4	20130213
731731	11:29:54	25:07:51	0.0209	94.0	16.42	16.02	···	S	Ha4	20130411
731760	11:33:26	24:52:23	0.0208	93.4	16.65	16.25	···	S	Ha4	20130412
731815	11:53:19	25:59:21	0.0181	79.9	20.29	20.12	···	lowSNR	Ha3	20130210
731846	11:58:37	25:27:02	0.0208	93.7	17.91	17.62	···	S	Ha4	20130411
732480	13:03:34	26:45:19	0.0339	149.1	17.08	16.61	11.03	S	Ha6	20130410
732624	13:24:07	25:10:59	0.0336	147.6	17.79	17.54	···	S	Ha5	20130214
732702	13:35:38	27:05:35	0.0363	159.2	16.50	15.89	9.49	S	Ha6	20130410
732729	13:39:04	24:40:33	0.0347	152.3	16.40	15.94	9.99	C	Ha6	20130411
732766	13:45:53	24:23:09	0.0351	153.9	17.45	17.03	10.78	S	Ha6	20130411
733362	15:00:32	27:13:23	0.0311	135.3	16.09	15.47	10.44	C	Ha5	20130410
733381	15:01:45	26:28:32	0.0307	133.7	16.09	15.51	10.82	lowSNR	Ha5	20130411
733411	15:03:23	26:40:20	0.0302	131.8	16.46	15.97	10.88	S	Ha5	20130411
733433	15:04:14	26:07:27	0.0311	135.3	16.30	15.75	10.73	lowSNR	Ha5	20130412
733463	15:04:48	26:10:22	0.0302	131.5	16.42	15.59	12.16	A	Ha5	20130410
733688	15:20:46	27:31:42	0.0322	139.9	16.27	16.05	11.36	S	Ha5	20130410
748722	22:51:47	14:18:39	0.0253	103.1	20.39	20.53	···	unknown	Ha4	20131010
748747	23:12:16	14:24:56	0.0386	160.3	20.00	19.64	···	unknown	Ha6	20131229
748783	00:14:56	14:12:52	0.0185	78.2	18.61	17.72	···	unknown	Ha3	20131229
748793	00:33:18	15:08:43	0.0314	129.7	19.22	18.67	···	unknown	Ha5	20131228
748821	01:48:47	14:37:59	0.0164	67.8	18.50	18.06	···	unknown	Ha3	20131231
748825	01:53:16	14:46:14	0.0263	108.7	18.73	18.54	···	unknown	Ha5	20131010
749389	08:36:24	25:18:38	0.0175	76.5	18.34	18.11	···	unknown	Ha3	20130208
749422	11:00:08	25:02:12	0.0201	90.8	22.08	20.88	···	unknown	Ha4	20130409

Here we give a brief description of how to get the sky background images. First, we subtracted all sources in the original image to get the object-masked image. Secondly, a median filter acted on the above image to fill the source regions with the surrounding sky in size of window 80×80 pixel^2. And then, if there were still unfilled regions, we smoothed it again. Finally, the background image was the median smoothed image and was subtracted from the original image.

The next step is to establish continuum-subtracted Hα images. For a galaxy, both pure Hα emission and stellar continuum contribute to Hα images. To get pure Hα emission, the scaled Hα images which continuum match that in R band subtract the R band image, the rest is considered as pure Hα flux. Under the assumption that field star only has continuum emission, the scaling parameter can be obtained by the statistical Wide to Narrow Continuum Ratio (WNCR), the ratio of a type of field stars' integral flux in R band to those in Hα band. Spector et al. (2012); Gavazzi et al. (2018) show that the WNCR is associated with types of star (OBAFGKS) as well as the color (e.g. $g-r$). This is the color effect (Spector et al. 2012). Following the method of continuum subtraction described in Lei et al. (2019), we choose the WNCR of the type of field stars whose color is same with the target galaxy, as the final WNCR of the image.

The galaxy photometry is obtained within the IRAF ellipse package which can provide a series of ellipse isophotes and total flux from center to outside of the galaxy. The R band image is used for detection of galaxy and getting photometry aperture. The semi-major axis and ellipticity are confirmed as photometry aperture when the mean isophote intensity reached 25 mag arcsec^{-2}. They are used in continuum-subtracted image to get Hα fluxes. The elliptical photometry radius (r_{25}) and ellipticity (e) can be found in Table 2. In Figure 3, we show four galaxies as a photometry example. From left to right are SDSS-, R band- and continuum-subtracted images. Photometry aperture is shown in yellow. All images are in the same size.

Flux correction includes Hα loss-, filter transmission-, extinction- and NII- correction. As Hα emission also contributes to the R band image, the Hα emission loss (4%) must be corrected (Lei et al. 2018). Not all of the Hα emission located in the high transmission part of the Hα filter. Each galaxy was made up for the transmission loss by the Hα filter transmission curve (Lei et al. 2018). The Galactic extinction was corrected

Table 2 The Star Formation Properties of Our Sample

AGC	r_{25} kpc	ellipse	$\log F_{H\alpha_{un}}$ erg cm^{-2} s^{-1}	$\log F_{H\alpha}$ erg cm^{-2} s^{-1}	logSFR $M_\odot yr^{-1}$	$\log\Sigma_{sfr}$ $M_\odot yr^{-1}kpc^{-2}$	$\log M_{HI}$ $M_\odot$	$\log\Sigma_{gas}$ $M_\odot pc^{-2}$	$\log M_*$ $M_\odot$	$\log\Sigma_*$ $M_\odot pc^{-2}$
(1)	(2)	(3)	(4)	(5)	(6)	(7)	(8)	(9)	(10)	(11)
43	11.34	0.59	$-13.147^{0.025}_{0.026}$	...	...	...	9.41	...	9.50	1.28
615	11.94	0.31	$-12.432^{0.030}_{0.033}$	$-12.443^{0.013}_{0.055}$	0.30	–2.19	9.49	0.80	10.81	2.32
619	26.57	0.76	$-13.546^{0.063}_{0.074}$	$-13.049^{0.003}_{0.043}$	0.39	–2.34	10.32	1.21	10.63	1.90
717	35.84	0.22	$-13.137^{0.299}_{1.986}$	$-13.198^{0.321}_{-\infty}$	0.19	–3.31	10.29	0.37	11.50	2.00
985	36.18	0.64	$-12.980^{0.175}_{0.297}$	$-12.818^{0.113}_{0.211}$	0.53	–2.64	10.34	0.79	11.42	2.25
1156	14.30	0.08	$-13.409^{0.101}_{0.132}$	$-13.293^{0.063}_{0.122}$	0.02	–2.75	10.19	0.99	10.39	1.62
1364	9.67	0.02	$-13.276^{0.047}_{0.053}$	$-13.280^{0.030}_{0.076}$	–0.61	–3.07	9.74	0.83	6.88	–1.58
1556	31.71	0.73	$-12.998^{0.324}_{-\infty}$	$-12.868^{0.250}_{0.870}$	–0.50	–3.43	9.72	0.36	10.90	1.97
1589	29.35	0.45	$-13.807^{0.499}_{-\infty}$	$-13.036^{0.121}_{0.228}$	0.42	–2.75	10.18	0.65	11.23	2.05
1630	10.89	0.59	$-12.311^{0.035}_{0.038}$	$-12.017^{0.001}_{0.040}$	0.53	–1.65	9.72	1.29	10.45	2.27
4167	11.02	0.42	$-13.094^{0.035}_{0.038}$	$-13.053^{0.014}_{0.056}$	–0.44	–2.78	9.77	0.97	9.18	0.84
4210	10.91	0.72	$-12.954^{0.048}_{0.054}$	$-12.739^{0.011}_{0.053}$	–0.04	–2.06	9.69	1.30	10.15	2.13
4275	18.79	0.18	$-12.464^{0.035}_{0.039}$	$-12.280^{0.005}_{0.046}$	0.63	–2.33	9.76	0.60	10.92	1.96
4456	20.16	0.19	$-12.258^{0.029}_{0.031}$	$-12.312^{0.015}_{0.057}$	0.47	–2.55	9.97	0.53	10.58	1.57
4509	22.71	0.50	...	...	...	...	9.46	...	10.74	1.83
4570	13.75	0.17	$-13.373^{0.070}_{0.084}$	$-13.241^{0.036}_{0.083}$	–0.31	–3.00	9.79	0.66	9.51	0.82
4597	16.15	0.37	$-12.536^{0.044}_{0.049}$	$-12.254^{0.005}_{0.045}$	0.70	–2.02	9.94	0.95	10.43	1.72
4602	18.18	0.63	$-14.600^{0.859}_{-\infty}$	$-13.429^{0.138}_{0.271}$	–0.62	–3.21	9.41	0.46	10.70	2.12
5189	24.79	0.50	$-11.876^{0.012}_{0.012}$	...	...	...	10.17	...	6.74	–2.24
5812	5.32	0.75	...	...	...	...	7.70	...	5.14	–2.21
6204	14.78	0.22	$-12.279^{0.018}_{0.018}$	$-12.088^{0.007}_{0.032}$	0.80	–1.92	9.70	0.87	10.51	1.78
6302	15.14	0.65	$-13.217^{0.117}_{0.162}$	$-12.585^{0.012}_{0.054}$	0.27	–2.13	9.82	1.13	10.45	2.05
6317	6.11	0.65	$-13.158^{0.055}_{0.063}$	...	...	...	9.10	...	8.89	1.27
6627	7.32	0.45	$-13.640^{0.088}_{0.110}$	...	...	...	9.04	...	9.36	1.39
6751	24.18	0.51	$-12.906^{0.066}_{0.077}$	$-12.853^{0.041}_{0.090}$	0.09	–2.87	10.11	0.73	9.09	0.14
6795	15.12	0.30	$-12.983^{0.049}_{0.055}$	$-12.937^{0.027}_{0.071}$	–0.06	–2.76	10.00	0.86	10.11	1.41
8911	22.62	0.18	$-13.037^{0.122}_{0.170}$	$-12.983^{0.094}_{0.173}$	0.40	–2.72	10.35	0.81	10.69	1.57
8927	23.54	0.68	$-11.864^{0.089}_{0.113}$	$-11.849^{0.070}_{0.133}$	1.17	–1.57	9.73	0.57	10.53	1.79
9679	21.67	0.58	$-13.266^{0.194}_{0.359}$	$-12.887^{0.076}_{0.142}$	0.35	–2.44	10.09	0.92	11.19	2.39
9830	4.31	0.10	$-12.028^{0.016}_{0.017}$	$-12.000^{0.003}_{0.036}$	–0.09	–1.81	8.89	0.73	4.12	–3.60
11948	21.21	0.37	$-13.398^{0.198}_{0.373}$	$-12.546^{0.016}_{0.058}$	0.50	–2.45	10.02	0.79	10.92	1.96
11992	9.07	0.25	$-13.170^{0.052}_{0.059}$	$-13.119^{0.029}_{0.074}$	–0.69	–2.97	9.69	0.96	9.51	1.23
12270	9.75	0.20	$-12.381^{0.077}_{0.094}$	$-12.488^{0.081}_{0.151}$	–0.52	–2.89	9.21	0.39	10.01	1.64
12481	8.67	0.08	$-12.207^{0.029}_{0.031}$	$-11.862^{0.005}_{0.034}$	0.72	–1.62	9.79	1.27	9.95	1.61
12519	16.00	0.67	$-12.370^{0.023}_{0.025}$	$-12.202^{0.003}_{0.037}$	0.37	–2.06	9.75	0.97	10.47	2.04
12705	11.96	0.49	$-13.136^{0.065}_{0.077}$	$-13.081^{0.041}_{0.090}$	–0.60	–2.96	10.04	1.23	9.70	1.35
12864	21.27	0.52	$-12.970^{0.112}_{0.151}$	$-12.622^{0.037}_{0.084}$	–0.00	–2.84	10.13	0.87	10.52	1.68
101934	16.82	0.46	$-13.883^{0.269}_{0.850}$	$-13.491^{0.115}_{0.216}$	–0.15	–2.83	10.01	0.92	10.97	2.29
102634	12.23	0.63	$-14.051^{0.091}_{0.115}$	...	...	...	9.66	...	9.54	1.30
102654	7.75	0.29	...	...	...	...	9.87	...	9.00	0.87
102735	1.69	0.19	$-14.361^{0.051}_{0.058}$	...	...	...	8.84	...	7.86	0.99
112457	2.79	0.04	$-13.219^{0.086}_{0.107}$	$-13.177^{0.062}_{0.121}$	–1.30	–2.68	8.23	0.44	9.00	1.62
113032	8.36	0.25	$-13.884^{0.034}_{0.037}$	...	...	...	9.51	...	9.26	1.05
113209	5.87	0.03	$-13.421^{0.025}_{0.027}$	$-13.322^{0.001}_{0.042}$	–0.25	–2.27	9.24	0.85	9.44	1.42
113800	16.39	0.36	$-14.148^{0.525}_{-\infty}$	$-12.793^{0.025}_{0.069}$	0.66	–2.07	10.08	1.12	10.95	2.22
121273	4.52	0.28	$-13.063^{0.041}_{0.045}$	$-12.868^{0.008}_{0.049}$	–0.43	–2.09	9.08	1.05	9.05	1.38
122141	3.27	0.32	$-13.002^{0.008}_{0.008}$	$-12.909^{0.013}_{0.026}$	–0.51	–1.87	9.02	1.23	6.99	–0.38
122217	2.11	0.67	$-14.475^{0.181}_{0.316}$	...	...	...	8.11	...	6.36	–0.31
122265	10.43	0.26	$-13.306^{0.034}_{0.037}$	$-13.079^{0.002}_{0.042}$	0.15	–2.26	9.60	0.87	9.91	1.51
122405	11.32	0.18	$-13.603^{0.053}_{0.060}$	...	...	...	9.40	...	10.47	1.95
122806	6.01	0.10	$-14.518^{0.064}_{0.075}$	...	...	...	9.61	...	7.92	–0.09
171483	4.06	0.26	$-14.317^{0.279}_{1.002}$	...	...	...	9.36	...	8.55	0.97
172836	6.55	0.66	$-14.186^{0.076}_{0.093}$	$-13.876^{0.021}_{0.064}$	–1.25	–2.92	8.86	0.79	8.86	1.20
174511	8.25	0.60	$-14.216^{0.058}_{0.068}$	...	...	...	9.74	...	9.29	1.35
174604	13.21	0.50	$-14.418^{0.108}_{0.144}$	...	...	...	9.82	...	9.03	0.59
174653	3.80	0.10	$-14.331^{0.224}_{0.486}$	...	...	...	9.05	...	6.89	–0.72
174720	3.12	0.35	$-13.918^{0.118}_{0.163}$	...	...	...	8.61	...	6.22	–1.08
180049	12.69	0.25	$-12.540^{0.047}_{0.053}$	$-12.193^{0.003}_{0.043}$	0.71	–1.87	9.39	0.91	10.65	2.06
180111	11.80	0.69	$-13.407^{0.021}_{0.022}$	$-13.013^{0.010}_{0.029}$	–0.12	–2.25	9.92	1.39	9.87	1.75
180612	16.42	0.12	$-12.854^{0.128}_{0.182}$	$-12.111^{0.008}_{0.049}$	0.78	–2.10	10.05	0.97	10.99	2.11
180649	11.21	0.31	$-13.222^{0.080}_{0.099}$	$-13.074^{0.042}_{0.091}$	–0.18	–2.62	9.62	0.77	9.88	1.45
180659	9.68	0.22	$-13.318^{0.022}_{0.024}$	$-13.201^{0.002}_{0.039}$	–0.30	–2.67	9.39	0.65	10.16	1.79
180939	9.78	0.09	$-13.707^{0.113}_{0.152}$	$-13.651^{0.085}_{0.158}$	–0.86	–3.29	9.61	0.72	9.49	1.05
181122	8.06	0.32	$-12.726^{0.025}_{0.027}$	$-12.531^{0.002}_{0.037}$	0.20	–1.95	9.23	0.94	10.16	2.02
181143	9.13	0.10	$-13.408^{0.093}_{0.119}$	$-13.086^{0.030}_{0.075}$	–0.29	–2.66	9.81	1.02	9.35	0.97
181774	9.51	0.41	$-13.670^{0.028}_{0.030}$	...	...	...	9.73	...	9.13	0.90

Table 2 *Continued.*

AGC	r_{25} kpc	ellipse	$\log F_{H\alpha_{un}}$ erg cm^{-2} s^{-1}	$\log F_{H\alpha}$ erg cm^{-2} s^{-1}	logSFR $M_\odot yr^{-1}$	$\log\Sigma_{sfr}$ $M_\odot yr^{-1}kpc^{-2}$	$\log M_{HI}$ $M_\odot$	$\log\Sigma_{gas}$ $M_\odot pc^{-2}$	$\log M_*$ $M_\odot$	$\log\Sigma_*$ $M_\odot pc^{-2}$
(1)	(2)	(3)	(4)	(5)	(6)	(7)	(8)	(9)	(10)	(11)
181925	9.96	0.27	$-13.775^{0.040}_{0.043}$	$-13.701^{0.015}_{0.058}$	–0.56	–2.91	9.65	0.85	9.10	0.74
182630	5.46	0.41	$-13.908^{0.038}_{0.042}$	···	···	···	9.09	···	5.72	–2.02
182736	11.63	0.70	$-13.864^{0.043}_{0.047}$	···	···	···	9.30	···	6.47	–1.63
182762	5.81	0.31	$-14.431^{0.056}_{0.064}$	···	···	···	9.25	···	8.97	1.11
182798	10.63	0.65	$-13.805^{0.048}_{0.054}$	···	···	···	9.64	···	9.67	1.57
182858	3.59	0.19	···	···	···	···	8.68	···	8.60	1.08
182859	4.89	0.34	$-13.245^{0.021}_{0.022}$	···	···	···	9.04	···	9.12	1.42
183012	4.63	0.49	$-14.803^{0.193}_{0.354}$	···	···	···	8.95	···	9.09	1.55
183074	7.99	0.54	$-13.966^{0.051}_{0.057}$	$-13.724^{0.011}_{0.053}$	–0.61	–2.57	9.45	1.08	9.53	1.57
183105	10.73	0.66	$-13.467^{0.024}_{0.025}$	$-13.425^{0.003}_{0.043}$	–0.52	–2.60	9.56	1.03	9.36	1.28
183127	8.88	0.37	$-13.033^{0.045}_{0.050}$	$-12.883^{0.014}_{0.056}$	0.03	–2.16	9.51	1.00	10.21	2.02
183135	9.15	0.57	$-14.074^{0.063}_{0.074}$	···	···	···	9.65	···	9.08	1.03
183419	8.55	0.50	$-13.430^{0.034}_{0.037}$	$-13.133^{0.001}_{0.039}$	–0.25	–2.31	8.98	0.75	9.97	1.91
183852	4.84	0.20	···	···	···	···	8.71	···	9.33	1.56
184340	3.58	0.25	$-14.231^{0.032}_{0.035}$	···	···	···	9.12	···	8.82	1.34
184444	4.64	0.12	$-14.170^{0.040}_{0.044}$	···	···	···	9.40	···	8.93	1.15
184450	4.13	0.37	$-12.782^{0.004}_{0.004}$	$-12.710^{0.016}_{0.023}$	0.02	–1.50	9.05	1.21	8.97	1.44
184559	4.68	0.03	$-13.808^{0.032}_{0.035}$	$-13.698^{0.007}_{0.048}$	–0.82	–2.64	9.26	1.01	9.26	1.44
188784	4.44	0.54	$-14.194^{0.065}_{0.077}$	···	···	···	9.01	···	8.53	1.08
203102	8.45	0.54	$-14.474^{0.116}_{0.159}$	···	···	···	9.48	···	9.01	0.99
203105	5.50	0.10	$-14.592^{0.067}_{0.080}$	···	···	···	9.60	···	8.92	0.99
210271	12.15	0.11	$-13.259^{0.048}_{0.053}$	$-13.226^{0.027}_{0.071}$	–0.30	–2.91	9.88	0.83	10.20	1.58
210653	10.36	0.26	$-12.820^{0.038}_{0.041}$	$-12.807^{0.019}_{0.061}$	0.10	–2.30	9.65	0.86	10.11	1.71
211188	11.56	0.77	$-13.921^{0.048}_{0.053}$	···	···	···	9.46	···	9.20	1.22
213028	3.15	0.14	$-13.919^{0.038}_{0.042}$	···	···	···	8.76	···	8.52	1.09
219344	3.51	0.40	$-14.534^{0.029}_{0.031}$	···	···	···	9.20	···	8.02	0.66
221378	12.61	0.15	$-12.970^{0.046}_{0.052}$	$-12.812^{0.015}_{0.057}$	0.58	–2.04	9.79	0.91	10.50	1.87
230107	17.19	0.22	···	···	···	···	9.67	···	10.87	2.01
230274	20.03	0.32	···	···	···	···	9.91	···	11.20	2.27
230488	29.93	0.19	$-12.932^{0.163}_{0.262}$	$-12.610^{0.069}_{0.131}$	0.78	–2.58	10.20	0.53	11.26	1.90
231669	13.84	0.45	$-12.958^{0.043}_{0.047}$	$-12.443^{0.005}_{0.034}$	0.93	–1.59	9.67	1.23	10.50	1.98
232123	13.00	0.46	$-14.138^{0.077}_{0.094}$	$-13.697^{0.011}_{0.053}$	–0.30	–2.76	9.80	0.95	10.06	1.61
234302	15.11	0.15	$-13.420^{0.149}_{0.228}$	$-13.121^{0.065}_{0.124}$	0.25	–2.54	10.13	0.96	10.70	1.91
234624	18.40	0.55	$-13.282^{0.094}_{0.120}$	$-12.956^{0.029}_{0.074}$	0.38	–2.30	9.56	0.70	10.63	1.95
234900	13.44	0.42	$-13.854^{0.287}_{1.196}$	$-13.551^{0.153}_{0.310}$	–0.19	–2.71	10.06	1.12	10.84	2.32
250004	18.65	0.26	$-12.790^{0.066}_{0.078}$	$-12.796^{0.050}_{0.102}$	0.49	–2.42	9.60	0.41	10.69	1.78
250348	12.68	0.04	$-13.230^{0.108}_{0.145}$	$-12.877^{0.034}_{0.081}$	0.36	–2.32	9.46	0.65	9.95	1.26
250802	14.07	0.06	$-12.771^{0.049}_{0.056}$	$-12.787^{0.034}_{0.080}$	0.51	–2.26	9.73	0.68	10.82	2.05
254523	11.13	0.41	$-14.030^{0.120}_{0.165}$	$-13.959^{0.088}_{0.163}$	–0.71	–3.07	9.76	0.95	8.89	0.53
320086	20.54	0.32	$-13.445^{0.149}_{0.228}$	$-13.076^{0.053}_{0.107}$	–0.11	–3.07	9.60	0.30	10.34	1.38
320265	14.93	0.76	$-13.335^{0.063}_{0.073}$	$-13.047^{0.015}_{0.057}$	–0.10	–2.33	9.72	1.12	10.17	1.95
320271	12.52	0.44	$-13.742^{0.283}_{1.091}$	$-13.668^{0.238}_{0.741}$	–0.91	–3.35	9.17	0.31	10.44	2.00
320276	16.65	0.46	$-12.862^{0.043}_{0.048}$	$-12.068^{0.012}_{0.027}$	1.30	–1.37	10.12	1.48	11.01	2.33
320488	16.42	0.17	$-13.056^{0.075}_{0.090}$	$-12.600^{0.009}_{0.050}$	0.77	–2.07	10.22	1.09	10.76	1.92
320513	18.41	0.33	$-13.232^{0.122}_{0.171}$	$-12.652^{0.018}_{0.060}$	0.77	–2.08	10.00	0.97	10.94	2.09
320527	18.72	0.78	$-13.291^{0.050}_{0.056}$	$-12.613^{0.008}_{0.031}$	0.39	–1.99	9.69	1.12	10.28	1.90
321072	9.59	0.35	$-13.769^{0.064}_{0.076}$	$-13.450^{0.014}_{0.056}$	–0.14	–2.41	9.68	1.03	9.80	1.53
321083	11.66	0.34	$-13.655^{0.067}_{0.080}$	$-13.481^{0.029}_{0.074}$	–0.18	–2.63	9.91	1.04	10.03	1.58
321104	6.64	0.43	$-13.270^{0.020}_{0.021}$	$-13.198^{0.002}_{0.038}$	–0.35	–2.25	9.23	0.93	9.54	1.64
321130	10.52	0.24	$-13.404^{0.054}_{0.062}$	$-13.087^{0.008}_{0.050}$	0.28	–2.14	9.52	0.89	10.22	1.79
321227	12.48	0.56	$-13.938^{0.077}_{0.094}$	···	···	···	9.52	···	9.28	0.95
321430	6.33	0.10	$-13.480^{0.024}_{0.025}$	$-13.377^{0.000}_{0.040}$	–0.48	–2.54	9.49	0.99	9.18	1.12
330039	15.92	0.40	$-13.032^{0.066}_{0.078}$	$-12.610^{0.008}_{0.049}$	0.35	–2.32	10.16	1.11	10.76	2.08
331061	7.71	0.38	$-13.686^{0.150}_{0.232}$	$-12.726^{0.001}_{0.041}$	0.11	–1.95	9.29	1.14	10.10	2.04
332140	7.51	0.62	$-14.068^{0.320}_{-\infty}$	···	···	···	9.65	···	8.05	0.22
332369	7.24	0.55	$-14.283^{0.058}_{0.067}$	···	···	···	9.58	···	9.28	1.41
332406	7.06	0.19	$-14.399^{0.064}_{0.075}$	···	···	···	9.38	···	9.02	0.92
332461	14.41	0.42	$-13.936^{0.200}_{0.382}$	$-13.622^{0.093}_{0.172}$	–0.22	–2.80	9.80	0.82	10.11	1.53
332628	10.96	0.51	···	···	···	···	10.01	···	9.50	1.24
332876	8.98	0.34	$-13.574^{0.017}_{0.017}$	···	···	···	9.54	···	8.58	0.35
719327	4.13	0.34	$-14.178^{0.119}_{0.165}$	···	···	···	9.06	···	8.96	1.41
721315	5.96	0.49	$-14.046^{0.055}_{0.063}$	$-13.828^{0.016}_{0.059}$	–1.04	–2.79	9.09	0.92	9.38	1.63
721317	9.13	0.40	$-13.711^{0.060}_{0.070}$	$-13.637^{0.034}_{0.081}$	–0.73	–2.93	9.33	0.70	9.68	1.49
722743	5.14	0.58	$-13.885^{0.059}_{0.069}$	$-13.717^{0.023}_{0.067}$	–0.80	–2.34	9.12	1.18	9.19	1.65
723579	6.56	0.66	$-13.699^{0.051}_{0.058}$	$-13.633^{0.027}_{0.071}$	–0.70	–2.37	9.21	1.12	9.22	1.55
724012	6.40	0.58	$-14.477^{0.090}_{0.113}$	···	···	···	9.27	···	8.88	1.15
724143	10.77	0.66	$-13.739^{0.061}_{0.071}$	$-13.510^{0.019}_{0.062}$	–0.69	–2.79	9.79	1.25	9.60	1.51

Table 2 *Continued.*

AGC	r_{25} kpc	ellipse	$\log F_{H\alpha_{un}}$ erg cm^{-2} s^{-1}	$\log F_{H\alpha}$ erg cm^{-2} s^{-1}	logSFR $M_\odot yr^{-1}$	$\log\Sigma_{sfr}$ $M_\odot yr^{-1}kpc^{-2}$	$\log M_{HI}$ $M_\odot$	$\log\Sigma_{gas}$ $M_\odot pc^{-2}$	$\log M_*$ $M_\odot$	$\log\Sigma_*$ $M_\odot pc^{-2}$
(1)	(2)	(3)	(4)	(5)	(6)	(7)	(8)	(9)	(10)	(11)
724186	7.66	0.68	$-14.175^{0.039}_{0.043}$	···	···	···	9.46	···	9.29	1.51
724236	4.97	0.60	$-14.263^{0.108}_{0.143}$	···	···	···	9.20	···	8.98	1.49
724244	8.88	0.53	$-13.381^{0.029}_{0.031}$	$-13.389^{0.011}_{0.053}$	–0.66	–2.73	9.28	0.77	9.51	1.44
724246	5.40	0.53	$-13.763^{0.041}_{0.046}$	···	···	···	9.10	···	9.02	1.38
725599	14.43	0.55	$-14.777^{0.573}_{-\infty}$	$-13.663^{0.067}_{0.128}$	–0.34	–2.81	9.70	0.85	10.22	1.75
725919	20.51	0.70	$-13.886^{0.248}_{0.639}$	$-13.008^{0.024}_{0.069}$	0.40	–2.20	9.98	1.09	7.98	–0.61
725935	11.49	0.61	$-14.320^{0.082}_{0.102}$	···	···	···	9.59	···	9.39	1.18
727048	19.02	0.60	$-13.869^{0.280}_{1.022}$	$-13.279^{0.075}_{0.141}$	–0.07	–2.73	9.79	0.77	10.24	1.59
727085	10.18	0.22	$-13.409^{0.040}_{0.044}$	$-13.313^{0.014}_{0.056}$	–0.02	–2.43	9.14	0.49	10.00	1.59
727112	16.44	0.40	$-12.961^{0.060}_{0.069}$	$-12.991^{0.047}_{0.098}$	0.30	–2.41	10.00	0.86	10.08	1.37
731528	9.99	0.39	$-14.441^{0.105}_{0.138}$	···	···	···	9.60	···	9.26	0.97
731598	12.67	0.68	$-14.050^{0.053}_{0.061}$	···	···	···	9.47	···	9.01	0.80
731690	8.32	0.46	$-13.572^{0.030}_{0.033}$	$-13.520^{0.009}_{0.050}$	–0.67	–2.73	9.36	0.86	9.52	1.45
731731	12.83	0.66	$-13.692^{0.045}_{0.051}$	$-13.655^{0.024}_{0.068}$	–0.73	–2.98	9.77	1.07	9.54	1.29
731760	11.03	0.52	$-14.090^{0.154}_{0.242}$	···	···	···	9.73	···	9.26	1.00
731815	4.66	0.21	$-13.971^{0.029}_{0.031}$	···	···	···	9.15	···	7.68	–0.06
731846	3.44	0.06	$-14.464^{0.064}_{0.075}$	···	···	···	8.98	···	8.89	1.35
732480	7.02	0.12	$-15.128^{0.608}_{-\infty}$	$-13.912^{0.058}_{0.113}$	–0.59	–2.72	9.53	1.01	9.87	1.74
732624	10.29	0.63	$-14.246^{0.042}_{0.047}$	···	···	···	9.76	···	9.22	1.14
732702	18.29	0.57	$-13.516^{0.059}_{0.068}$	$-13.146^{0.008}_{0.049}$	0.23	–2.42	10.05	1.03	10.40	1.74
732729	15.63	0.62	$-13.471^{0.091}_{0.115}$	$-13.264^{0.042}_{0.091}$	0.08	–2.39	9.98	1.12	10.18	1.72
732766	8.21	0.46	$-13.835^{0.075}_{0.091}$	$-13.582^{0.026}_{0.070}$	–0.23	–2.29	9.87	1.40	9.71	1.65
733362	11.23	0.14	$-13.706^{0.155}_{0.243}$	$-13.494^{0.086}_{0.159}$	–0.26	–2.79	9.64	0.73	10.34	1.81
733381	14.70	0.24	$-13.955^{0.260}_{0.747}$	$-13.658^{0.137}_{0.266}$	–0.43	–3.14	9.89	0.75	10.14	1.43
733411	15.60	0.46	$-14.190^{0.264}_{0.792}$	$-13.720^{0.094}_{0.173}$	–0.50	–3.12	9.50	0.50	9.86	1.25
733433	11.79	0.19	$-14.058^{0.263}_{0.775}$	$-13.660^{0.110}_{0.205}$	–0.42	–2.97	9.67	0.72	10.15	1.60
733463	7.37	0.03	$-14.395^{0.417}_{-\infty}$	$-14.181^{0.288}_{-\infty}$	–0.97	–3.19	9.37	0.73	10.47	2.26
733688	11.63	0.38	$-13.224^{0.044}_{0.049}$	$-13.187^{0.023}_{0.067}$	0.08	–2.34	9.95	1.09	9.79	1.37
748722	6.90	0.30	$-14.430^{0.178}_{0.307}$	···	···	···	9.60	···	7.67	–0.35
748747	3.12	0.09	$-15.122^{0.105}_{0.138}$	···	···	···	9.57	···	8.03	0.59
748783	2.71	0.42	$-14.758^{0.095}_{0.121}$	···	···	···	9.14	···	8.85	1.73
748793	4.83	0.10	$-15.123^{0.154}_{0.242}$	···	···	···	9.35	···	8.96	1.14
748821	4.22	0.63	$-14.559^{0.064}_{0.075}$	···	···	···	8.98	···	8.25	0.94
748825	4.30	0.10	$-15.309^{0.163}_{0.265}$	···	···	···	9.32	···	8.62	0.90
749389	3.54	0.33	$-14.352^{0.024}_{0.025}$	···	···	···	9.23	···	8.34	0.92
749422	7.02	0.65	$-14.657^{0.121}_{0.168}$	···	···	···	9.19	···	8.42	0.69

using the Schlegel et al. (1998) map and the extinction curve from Fitzpatrick (1999). The intrinsic extinction was derived from the linear relationship $L(H\alpha)_{corr} = L(H\alpha)_{obs} + 0.038\nu L_\nu(12\,\mu m)$ (Wen et al. 2014), which is more suitable for the whole galaxy correction, a detailed discussion of intrinsic extinction is given in Section 4. [NII] correction was based on the ratio ([NII]/Hα) from MPA-JHU measurements.

The flux of R-band images was calibrated using the field stars cross-matched with SDSS DR7 psfMag. For calibration, we use the magnitude in SDSS r- and i-band to Johnson R-band, $R = r - 0.2936(r - i) - 0.1439$ (Lupton et al. 2005).

2.4 Ancillary Data

NASA' Wide-field Infrared Survey Explorer (WISE) (Wright et al. 2010) has mapped all-sky at four mid-infrared bands W1, W2, W3, W4 (3.4-, 4.6-, 12- and 22- μm). The all-sky surveys are done by using a 40cm telescope after its launch on 2009 December 14. The angular resolution is $6''.1$, $6''.4$, $6''.5$, $12''.0$ from W1 to W4 band. The point source sensitivities of W1, W2, W3 and W4 in Vega magnitude are 16.5, 15.5, 11.2 and 7.9, when 5σ is achieved. Of the galaxies in our sample, 99%, 95%, 62% and 43% have W1, W2, W3 and W4 counterparts with $S/N > 3$, respectively. The W3 band magnitude is given in Table 1.

Sloan Digital Sky Survey (SDSS) is one of the most successful sky survey providing the photometric and spectroscopic data. As the sky region of SDSS have overlapped with the ALFLFA, all galaxies of our sample have g and r band Petro magnitude from SDSS DR12 which are given in Table 1.

MPA-JHU refers to a set of spectrum lines measurements from SDSS data releases by the Max Planck Institute for Astrophysics and the Johns Hopkins University group. Those fluxes, including Hα, Hβ, [NII], [OIII]..., are derived from the galaxy central within 3 arcsec fiber apertures. Of the galaxies in our sample, 74%, 71% and 71% has Hα, Hβ and [NII] flux with $S/N > 3$, respectively.

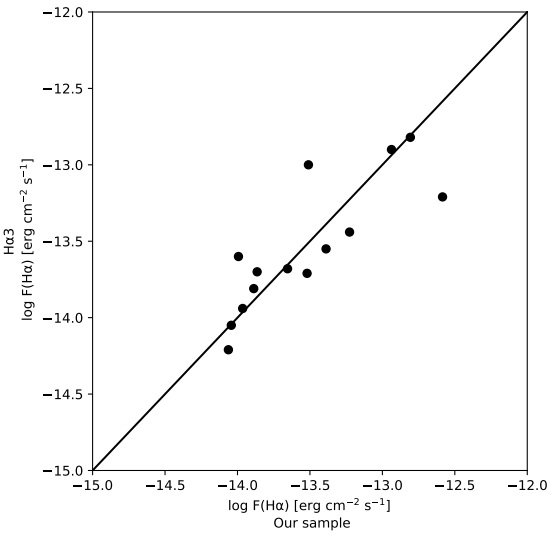

Fig. 4 Comparison of Hα fluxes for galaxies in our work with those of Gavazzi et al. (2015a).

3 THE Hα CATALOG

Here we briefly discuss the parameters we have listed in Table 2. We provide the observation Hα flux with ($F_{H\alpha}$) and without ($F_{H\alpha_{un}}$) dust corrected. A statistical Hα flux with dust corrected comparison between our sample and Hα3 is shown in Figure 4. Gavazzi et al. (2015a) present Hα3 (acronym for H$\alpha-\alpha\alpha$), an Hα imaging survey of the galaxies in Coma Supercluster that are also selected from ALFALFA. In Figure 4, all matched objects show a good agreement with comparison sample with 0.19 standard deviation of the differences.

The SFR is calculated from the following formula, $SFR_{H\alpha}(M_\odot\ yr^{-1}) = 7.9\times10^{-42}[L(H\alpha)](erg\ s^{-1})$ (Kennicutt 1998). The L(Hα) is derived from the Hα flux after IR-based dust correction. The initial mass function used in the conversion is a Salpeter function $[dN(m)/dm = -2.35]$ over m=0.1–100 $M_\odot$. The star formation surface density (Σ_{SFR}), in units $M_\odot yr^{-1}kpc^{-2}$, is calculated using $\Sigma_{SFR} = SFR/(\pi ab)$. Here, a and b are ellipse photometry radius.

The gas mass contains HI and H_2 mass. The HI mass is from α.40 catalog and the H_2 mass is derived by using $logM_{H_2}(CO_{2-1}) = (1.03\pm0.06)logL_{12\,\mu m}\pm(-0.12\pm0.48)$ which is based on the sample of 32 nearby gas rich star-forming galaxies selected from ALFALFA and WISE (Jiang et al. 2015). The HI mass surface density ($\Sigma_{HI} = M_{HI}/(\pi 1.7^2 ab)$). It is difficult to obtain HI radius. In general, HI radius is larger than the optical radius, the average ratio of HI to optical radius is about 1.7±0.5 and the ratio does not depend on morphological type and luminosity (Broeils & Rhee 1997; Jaskot et al. 2015). Following Jaskot et al. (2015), we use $1.7r_{25}$ instead of r_{HI}.

The stellar mass of our sample is derived from the g-i color and i-band luminosity using the formula $log_{10}(M_*/L_i) = -0.152+0.518(g-i)$ (Bell et al. 2003). The stellar mass surface density, $\Sigma_* = M_*/\pi ab$, here a and b are also from optical photometric.

4 Hα EMISSION LINE & MID-INFRARED(MIR) RELATION

The dust absorbed short wavelengths (UV) energy and emitted at a longer wavelength, e.g. mid-IR, radio. Earlier studies suggest a tight relation between mid-IR and other ongoing star formation tracers (Wu et al. 2005; Calzetti et al. 2005, 2007; Zhu et al. 2008; Kennicutt et al. 2009; Zhu et al. 2010; Hao et al. 2011; Wen et al. 2014; Zhu et al. 2019). Wen et al. (2014) show the extinction-corrected Hα luminosity ($L_{H\alpha}$) has a tighter relation with linear combinations of the luminosity of extinction-uncorrected Hα ($L_{H\alpha(obs)}$) and mid-IR (W3, W4) than those with pure mid-IR. So Wen et al. (2014) provide another way to construct dust-corrected $L_{H\alpha}$. We explore whether our sample is still applicable to this relationship.

Figure 5 presents the correlations between MIR (W3, W4) and Hα luminosity, here the $L_{H\alpha}$ is after the Galactic and internal extinction-corrected. The dust corrected $L_{H\alpha}$ was obtained by the integrated Balmer decrement derived from MPA-JHU measurements. The upper panels show the correlations between rest-frame W3, W4 luminosity and Hα luminosity without dust corrected ($L_{H\alpha(obs)}$). In the upper panels, the black lines are from Wen et al. (2014) which were derived based on star-forming the galaxies matching SDSS and WISE. The lower panels show the linear combination of uncorrected Hα and IR (12, 22 μm) luminosity compared with the same extinction-corrected Hα luminosity, $L_{H\alpha(corr)} = L_{H\alpha(obs)} + \eta L_{IR}$, the coefficient η=0.038 is from Wen et al. (2014).

Four objects (AGCN 4602, 113800, 331061, 732480) in panel (d) shown in red solid circles in our sample deviate 2σ away from the correlations. As the relation was derived based on star-forming galaxies, we checked whether the outliers are AGN. Figure 6 is the BPT diagnostic diagram of our sample. The three spectral types of galaxies (AGN, composite galaxies, star-forming galaxies) are classified by the traditional "Baldwin, Phillips & Terlevich" (BPT) diagram (Baldwin et al. 1981; Veilleux & Osterbrock 1987; Kauffmann et al. 2003). Based on emission lines measurements in MPA-JHU, our sample was classified into 97 star-forming galaxies (blue stars), 11 composites (green solid circles), eight AGN (red solid pentagons), nine galaxies (grey pluses) with lower S/N< 3 and 44 unknown. The types are given in Table 1. In Figure 5, all

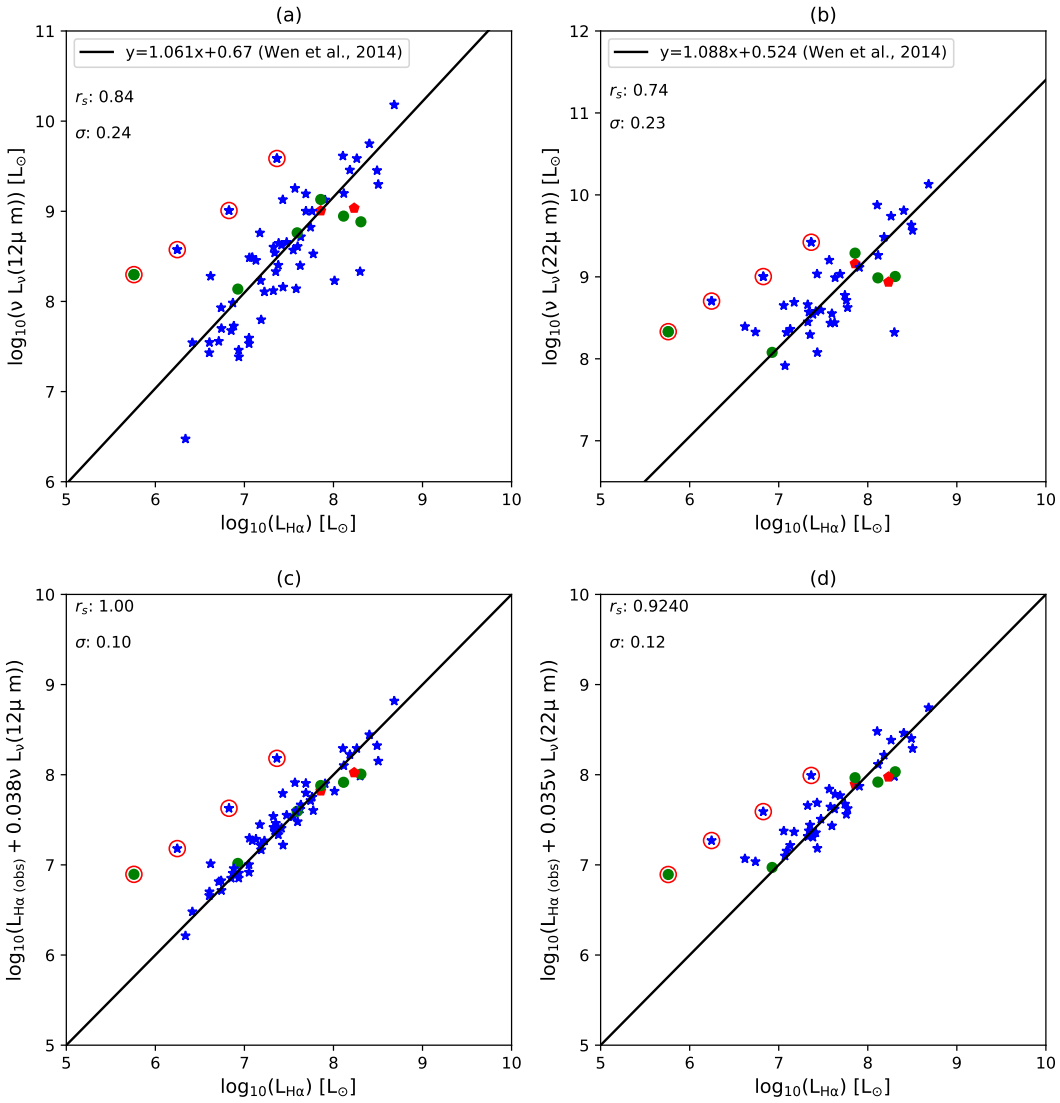

Fig. 5 The relation between 12, 22 μm infrared (IR) luminosity and dust-corrected Hα luminosity for our sample. $L_{H\alpha(obs)}$ is the Hα luminosity without dust-corrected. The dust-corrected Hα luminosity ($L_{H\alpha}$) were derived from the integrated Balmer decrement. The solid black lines in upper panels are fitted line from Wen et al. (2014). All symbols definition follows BPT diagnostic diagram in Fig. 6. All symbols with red open circles are outliers which deviate more than 2 σ away from the line in panel (c). r_s present the Spearman rank-order correlation analysis coefficient of the x- and y- axis. σ show the deviation from the line.

symbols definitions follow Figure 6. Among the galaxies with higher S/N in our sample, 84% of them are star-forming galaxies. After checking, all the outlier objects (symbols with red open circles) above the line are with lower Hα image signal to noise ratio (SNR) and they are not AGN.

The Spearman's rank-order correlation coefficient (r_s) measures how well the relationship between two variables. A perfect Spearman's rank-order correlation coefficient is $\pm$1. In Figure 5, the value of r_s show the relationship after clipping deviation objects. We confirm that the extinction-corrected Hα luminosity have correlations with restframe 12 and 22 μm, have most perfect relation with $L_{H\alpha(obs)} + 0.038\nu L_\nu(12\,\mu m)$ from Wen et al. (2014) among four panels , whose Spearman is 1 and deviation σ is 0.1, this relation can be used to estimate the intrinsic extinction. Following this method, we derive the dust-corrected $L_{H\alpha}$ and list them in Table 2.

5 GAS AND STAR FORMATION IN GALAXIES

5.1 The SFR in HI Detected Galaxies

We collect other available galaxies together with our sample in α.40 to study the correlations among M_*, M_{HI}

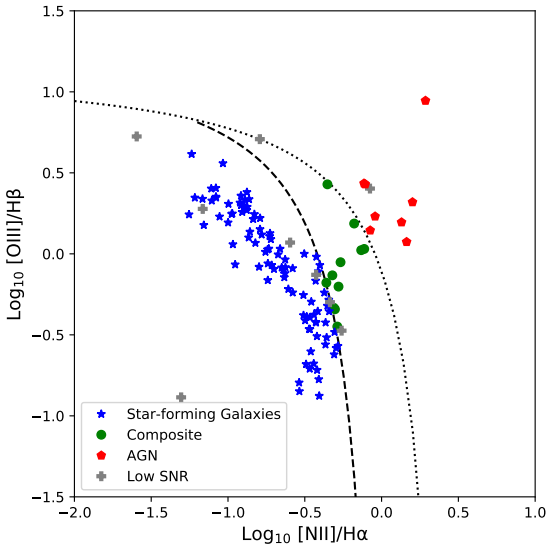

Fig. 6 The BPT diagnostic diagram of our sample.

and SFR. This sample is in a vast range of stellar mass, from low stellar mass dwarf galaxies and galaxies in Virgo cluster, to LSBGs, to larger stellar mass of galaxies in Coma cluster and our sample. In Figure 7, the green and red pluses show the galaxies from the Virgo cluster (Gavazzi et al. 2012) and Coma clusters (Gavazzi et al. 2015a), respectively. The dwarf galaxies shown as purple pluses derive from (Huang et al. 2012a). The grey open circles show the LSBGs from Lei et al. (2018, 2019). The black open circles are our sample. The HI mass of all galaxies derive from ALFALFA.

In panel (a), there is a trend that HI mass increases with stellar mass, but this cannot be described by linear relation, the slope slows down at the higher stellar mass. The one-to-one relation is given with a dashed line. In panel (e), M_{HI}/M_* increases with decreasing M_*, some of the higher stellar mass have lower gas fraction. Huang et al. (2012a) explained this is consistent with the idea that the massive galaxies experience AGC feedback which moves the gas lead to a lower gas fraction.

In panel (b), we confirm the well-known correlation that the SFR increases with stellar mass (Brinchmann et al. 2004; Bothwell et al. 2009). Figure 7(f) shows the plots of the sSFR–M_* correlation. The blue diamonds are average sSFR within 1 stellar mass bin in the logarithmic axis derived from our sample and comparison sample. In general, sSFR decreases with increasing stellar mass. However this trend is crude especially at low M_* ($M_* < 10^9$ $M_\odot$) region due to the small size of the sample and most of dwarf galaxies with large dispersion in sSFR. At the high mass end, a turnover can be seen supporting the idea that the sSFR dropped sharply when stellar masses close to the transition mass $10^{10.3\sim10.5}M_\odot$ (Salim et al. 2007; Bothwell et al. 2009), and for reference a grey dashed line has been drawn. We overplot the star formation (SF) sequence with a black dotted line defined by Schiminovich et al. (2007). It is no surprise to see that the galaxies in our sample are in agreement with star-forming sequence defined by previous work, as most of galaxies in our sample are star-forming galaxies.

In panel (c), SFR also increases with HI mass as well the stellar mass which is consistent with the results in Huang et al. (2012a). It is hard to see a clear trend in the relationship between sSFR and M_{HI} in panel (g).

Panel (d) suggests that SFR/M_{HI} has a weak increasing function of M_* with large dispersion. According to the results in Parkash et al. (2018), HI-selected and stellar mass-selected sample show different in SFR/M_{HI} versus M_* relation. HI -selected sample and all galaxies in panel (d) show an increasing SFR/M_{HI} with M_* (Jaskot et al. 2015; Lutz et al. 2017). However, stellar mass-selected sample exhibits a constant SFR/M_{HI} with M_* (Schiminovich et al. 2010; Wong et al. 2016). All galaxies in panel (d) consist with the HI-selected sample from Parkash et al. (2018) in SFR/M_{HI} versus M_* relation. In panel (h), there is no clear systematic trend between SFR/M_{HI} and M_{HI}. Although our sample and LSBGs occupy a similar region in M_{HI}, our sample has a higher SFR/M_{HI} compared to LSBGs indicating that it is difficult for LSBG to effectively convert the HI gas to stars.

5.2 Star Formation Law

5.2.1 K-S law

The empirical relationship between the SFR and gas is the K-S law, $\Sigma_{SFR} \propto \Sigma_{gas}^{1.4}$. But K-S law cannot hold all types of galaxies, especially LSBGs which in low gas surface density regions. de los Reyes & Kennicutt (2019) update K-S law using more accurate measurements of Σ_{SFR} and larger sample with local quiescent spiral, dwarf, and LSBGs. Figure 8 shows the relationship between Σ_{SFR} and Σ_{gas} for our sample (black open circles). The K-S law (black solid line) is fitted by star forming galaxies (blue solid circles) and starburst galaxies(green solid circles). The revised K-S law for spiral galaxies alone shown in the purple line is described by a $n = 1.41$ power law, similar to K-S law. There is a tiny difference between K-S law and revised K-S law for our sample (black open circles). The stddev of deviation from our sample to K-S law and revised K-S law are 0.1341 and 0.1412, respectively. Our sample is well described by K-S law as well as revised K-S law. However, it is easy to see that neither K-S law nor revised

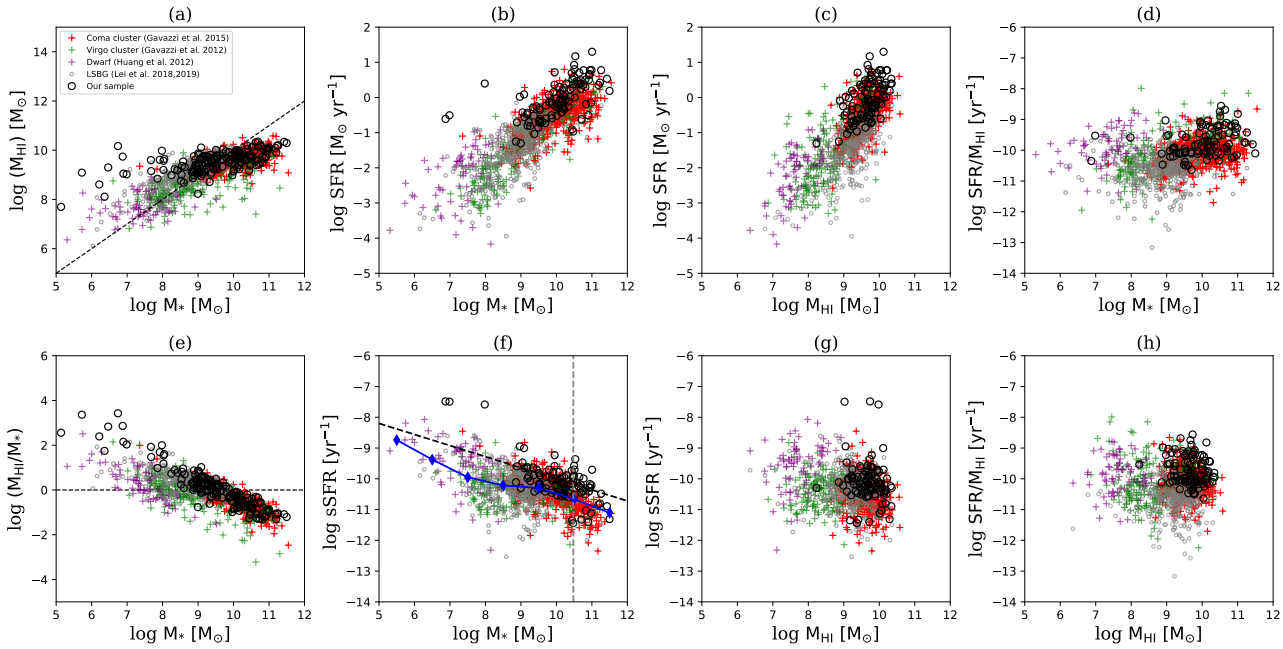

Fig. 7 The correlations among M_*, M_{HI} and SFR. All symbols are galaxies belong to ALFALFA. Red and green pluses indicate the Hα image observed galaxies from Coma and Virgo cluster, respectively (Gavazzi et al. 2015a, 2012). Purple pluses are dwarf galaxies from Huang et al. (2012a). Grey open circles are LSBGs from Lei et al. (2018, 2019). Our sample is shown in black open circles. Blue diamonds denote the average sSFR in each log y bin with 1 dex.

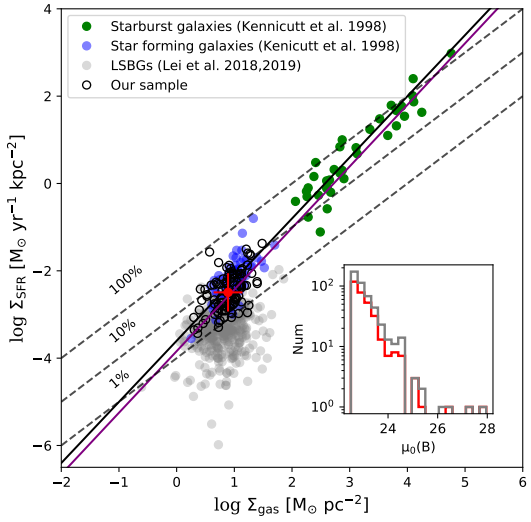

Fig. 8 The relation between Σ_{SFR} and Σ_{gas}. The black solid line is K-S law which is fitted on the star forming galaxies (*blue solid circles*) and starburst galaxies (*green solid circles*). The purple solid line is the revisiting K-S law only for star-forming galaxies. The grey solid circles are LSBGs from Lei et al. (2019). The red solid circle shows the mean value of Σ_{SFR} and Σ_{gas} of our sample, and the error bars present the deviation within 1 σ. The subfigure is the histogram of μ_0(B). In the subfigure, the grey line and red line present LSBGs from Lei et al. (2018, 2019) and "real LSBG sample" defined by Σ_{SFR}.

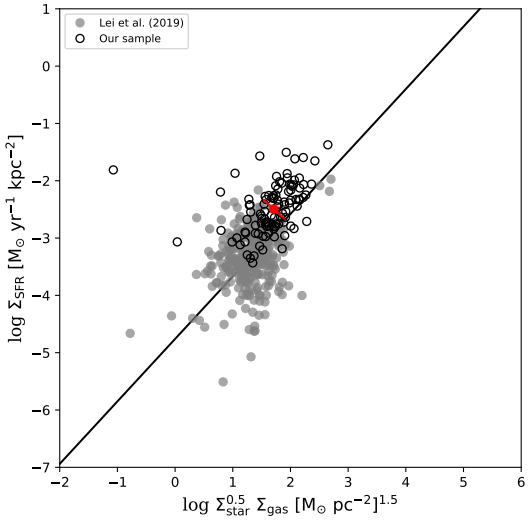

Fig. 9 The star formation relation between Σ_{SFR} and $\Sigma_*\Sigma_{gas}$. The black solid line is revised extended Schmidt law. Another LSBGs sample from Lei et al. (2018, 2019) is shown in grey solid circles. The black open circles indicate our sample.

K-S law is able to describe the LSBGs (grey solid circles) well.

LSBGs are defined as galaxies with surface brightness fainter than a certain threshold value, for example the

LSBGs in Figure 8 whose central surface brightness in B band ($\mu_0(\mathrm{B})$) is greater than 22.5 $\mathrm{mag\ arcsec^{-2}}$. Their counterparts with higher surface brightness are considered as high surface brightness galaxies (HSBGs). However, it is difficult to link the classification to fundamental physical parameters, such as stellar mass, star formation and angular momentum, and star formation rate surface density$\cdots$. As shown in Figure 8, the Σ_{SFR} in our sample is much higher than that in LSBGs, so we try to figure out if this classification is linked to the Σ_{SFR}. The red solid circle shows the central of our sample (or HSBGs) and the error bars show the deviation within 1 σ. We refer to the LSBGs whose Σ_{SFR} is lower than the lower limits of HSBGs as "real LSBG sample" to distinguish it from the LSBG sample (grey solid circles). The "real LSBG sample" are expected for a higher $\mu_0(\mathrm{B})$. Beyond our expectation, the histograms of $\mu_0(\mathrm{B})$ show no differences between "real LSBG sample" (red line) and LSBG sample (grey line) from Lei et al. (2018, 2019). So Σ_{SFR} is not suitable in classification of LSBGs.

5.2.2 *extended Schmidt law*

In addition to K-S law, another scaling law has been proposed: Shi et al. (2011, 2014, 2018) proposed relationships between SFR and a combination of gas and stellar mass. It is called extended Schmidt law which aims to be suitable for more galaxies, especially for faint objects (LSBGs, outer of the galaxy). The extended Schmidt law, $\Sigma_{\mathrm{SFR}}/\Sigma_{\mathrm{gas}} = 10^{-10.28\pm0.08}\Sigma_{\mathrm{star}}^{0.48\pm0.04}$, is the best fit line for six types of galaxies which are late-type galaxies, early-type galaxies, LSB galaxies, local luminous infrared galaxies (z=0-LIRGs), high-redshift star-forming galaxies (High-z SFGs) and high-redshift merging sub-millimeter galaxies (High-z SMG) (Shi et al. 2011). Shi et al. (2018) revisited extended Schmidt law as $\Sigma_{\mathrm{SFR}} \propto (\Sigma_{\mathrm{star}}^{0.5}\Sigma_{\mathrm{gas}})^{1.09}$, which is suitable for more types of objects from the fainter outer disk of galaxies, to merging galaxies, to molecular clouds... In Figure 9, the black open circles and grey solid circles are our sample and LSBGs from Lei et al. (2018, 2019), respectively. The black solid line is the updated extended Schmidt law.

After 3 σ clipping, the median offset of LSBGs around the extended Schmidt law with 0.0020 dex is smaller than that of our sample with 0.2700 dex. The standard deviation of LSBGs and our sample from the extended Schmidt law are 0.3677 dex and 0.2345 dex, respectively. This confirms that LSBGs show reduced deviation from extended Schmidt law. However, they still present a relatively large scatter.

The red point represents the center of our sample (black open circles), which is defined as the mean value after 3 σ clipping. Our sample presents a standard deviation with 0.2345 dex, which is smaller than the distance of 0.2700 dex from a red point to extend Schmidt law, which indicate that our sample is above the extend Schmidt law, deviates the extend Schmidt law. The scatter of our sample around the revised extended Schmidt law is 0.2345 dex, larger than 0.1341 dex around the K-S law, larger than 0.1412 dex around the revised K-S law. So our sample follows the K-S law as well as the revised K-S law than the extended Schmidt law.

6 SUMMARY

We observed the Hα images of 169 un-LSBGs from ALFALFA to derive their star formation properties, combining photometric and spectroscopic data from SDSS and WISE. We have presented a catalog containing Hα flux, SFR, Σ_{SFR}, $\mathrm{M_{HI}}$, $\mathrm{M_{gas}}$, Σ_{gas}, $\mathrm{M_*}$, $\Sigma_{\mathrm{M_*}}$. Based on MPA-JHU measurements, our sample contains 97 star-forming galaxies, 11 composites, eight AGN, nine low SNR galaxies and 44 unknown galaxies. Combing the mid-IR band data, we confirm that $\mathrm{L_{H\alpha(obs)}} + 0.038\nu\mathrm{L}_\nu(12\,\mu\mathrm{m})$ has a tight correlation with MPA-based $\mathrm{L(H\alpha)_{corr}}$ in our sample. By the help of the above relationship, we derived the instinct extinction.

The correlations among $\mathrm{M_*}$, HI content and SFR are confirmed as below: the $\mathrm{M_{HI}/M_*}$ decrease with the $\mathrm{M_*}$, low stellar mass galaxies have rich HI reservoir. All of the galaxies show linear relation in SFR versus $\mathrm{M_*}$. In the relationship between sSFR versus $\mathrm{M_*}$, the galaxies with higher $\mathrm{M_*}$ show a noted characteristic transition at $\sim 3\times10^{10}\mathrm{M}_\odot$. Our sample is agreement with star-forming sequence defined by previous works. There is a trend that $\mathrm{SFR/M_{HI}}$ increases with $\mathrm{M_*}$ with larger dispersion. Neither sSFR nor $\mathrm{SFR/M_{HI}}$ shows good correlation with $\mathrm{M_{HI}}$. As most of galaxies in our sample are star-forming galaxies, they tend to show a tight correlation with revised K-S law as well as K-S law.

Acknowledgements This project is supported by the National Natural Science Foundation of China (Grant Nos. 12003043, 11733006, 12090041, 12090040, 12073035, 11890693 and U1931109) and the National Key R&D Program of China (No. 2017YFA0402704). We acknowledge the support of the staff of the Xinglong 2.16 m telescope. This work was partially supported by the Open Project Program of the Key Laboratory of Optical Astronomy, National Astronomical Observatories, Chinese Academy of Sciences. We acknowledge the work of the entire ALFALFA collaboration team in observing, flagging and extracting the catalog of galaxies used in this work. The ALFALFA team at Cornell is supported by NSF grant AST-0607007 and AST-1107390 and by grants from the Brinson Foundation. We thank the useful SDSS database and the MPA/JHU catalogs. Funding for

the SDSS has been provided by the Alfred P. Sloan Foundation, the Participating Institutions, the National Science Foundation, the U.S. Department of Energy, the National Aeronautics and Space Administration, the Japanese Monbukagakusho, the Max Planck Society, and the Higher Education Funding Council for England. We used data products from the Wide-field Infrared Survey Explorer, which is a joint project of the University of California, Los Angeles, and the Jet Propulsion Laboratory/California Institute of Technology, founded by the National Aeronautics and Space Administration.

References

Baldwin, J. A., Phillips, M. M., & Terlevich, R. 1981, PASP, 93, 5
Bell, E. F., McIntosh, D. H., Katz, N., et al. 2003, ApJS, 149, 289
Bigiel, F., Leroy, A., Walter, F., et al. 2008, AJ, 136, 2846
Bothwell, M. S., Kennicutt, R. C., & Lee, J. C. 2009, MNRAS, 400, 154
Brinchmann, J., Charlot, S., White, S. D. M., et al. 2004, MNRAS, 351, 1151
Broeils, A. H., & Rhee, M. H. 1997, A&A, 324, 877
Calzetti, D., Kennicutt, R. C., J., Bianchi, L., et al. 2005, ApJ, 633, 871
Calzetti, D., Kennicutt, R. C., Engelbracht, C. W., et al. 2007, ApJ, 666, 870
de los Reyes, M. A. C., & Kennicutt, Robert C., J. 2019, ApJ, 872, 16
Du, W., Cheng, C., Wu, H., et al. 2019, MNRAS, 483, 1754
Du, W., Wu, H., Lam, M. I., et al. 2015, AJ, 149, 199
Fan, Z., Wang, H., Jiang, X., et al. 2016, PASP, 128, 115005
Fitzpatrick, E. L. 1999, PASP, 111, 63
Fossati, M., Gavazzi, G., Savorgnan, G., et al. 2013, A&A, 553, A91
Gavazzi, G., Consolandi, G., Pedraglio, S., et al. 2018, A&A, 611, A28
Gavazzi, G., Fumagalli, M., Fossati, M., et al. 2013a, A&A, 553, A89
Gavazzi, G., Fumagalli, M., Galardo, V., et al. 2012, A&A, 545, A16
Gavazzi, G., Pierini, D., & Boselli, A. 1996, A&A, 312, 397
Gavazzi, G., Savorgnan, G., Fossati, M., et al. 2013b, A&A, 553, A90
Gavazzi, G., Consolandi, G., Viscardi, E., et al. 2015a, A&A, 576, A16
Gavazzi, G., Consolandi, G., Dotti, M., et al. 2015b, A&A, 580, A116
Giovanelli, R., Haynes, M. P., Kent, B. R., et al. 2005a, AJ, 130, 2598
Giovanelli, R., Haynes, M. P., Kent, B. R., et al. 2005b, AJ, 130, 2613
Hao, C.-N., Kennicutt, R. C., Johnson, B. D., et al. 2011, ApJ, 741, 124
Haynes, M. P., Giovanelli, R., Martin, A. M., et al. 2011, AJ, 142, 170
Huang, S., Haynes, M. P., Giovanelli, R., et al. 2012b, ApJ, 756, 113
Huang, S., Haynes, M. P., Giovanelli, R., et al. 2012a, AJ, 143, 133
Jaskot, A. E., Oey, M. S., Salzer, J. J., et al. 2015, ApJ, 808, 66
Jaskot, A., Oey, S., Salzer, J., et al. 2016, in From Interstellar Clouds to Star-Forming Galaxies: Universal Processes?, eds. P. Jablonka, P. André, & F. van der Tak, 315, E37
Jiang, X.-J., Wang, Z., Gu, Q., Wang, J., & Zhang, Z.-Y. 2015, ApJ, 799, 92
Kauffmann, G., Heckman, T. M., Tremonti, C., et al. 2003, MNRAS, 346, 1055
Kennicutt, Robert C., J. 1998, ApJ, 498, 541
Kennicutt, Robert C., J., Hao, C.-N., Calzetti, D., et al. 2009, ApJ, 703, 1672
Kennicutt, R. C., & Evans, N. J. 2012, ARA&A, 50, 531
Krumholz, M. R. 2012, ApJ, 759, 9
Lei, F.-J., Wu, H., Zhu, Y.-N., et al. 2019, ApJS, 242, 11
Lei, F.-J., Wu, H., Du, W., et al. 2018, ApJS, 235, 18
Lupton, R. H., Jurić, M., Ivezić, Z., et al. 2005, in Bulletin of the American Astronomical Society, 37, 1384
Lutz, K. A., Kilborn, V. A., Catinella, B., et al. 2017, MNRAS, 467, 1083
McGaugh, S. S. 1994, ApJ, 426, 135
Parkash, V., Brown, M. J. I., Jarrett, T. H., & Bonne, N. J. 2018, ApJ, 864, 40
Salim, S., Rich, R. M., Charlot, S., et al. 2007, ApJS, 173, 267
Salpeter, E. E. 1955, ApJ, 121, 161
Schiminovich, D., Wyder, T. K., Martin, D. C., et al. 2007, ApJS, 173, 315
Schiminovich, D., Catinella, B., Kauffmann, G., et al. 2010, MNRAS, 408, 919
Schlegel, D. J., Finkbeiner, D. P., & Davis, M. 1998, ApJ, 500, 525
Shi, Y., Armus, L., Helou, G., et al. 2014, Nature, 514, 335
Shi, Y., Helou, G., Yan, L., et al. 2011, ApJ, 733, 87
Shi, Y., Yan, L., Armus, L., et al. 2018, ApJ, 853, 149
Spector, O., Finkelman, I., & Brosch, N. 2012, MNRAS, 419, 2156
Van Sistine, A., Salzer, J. J., Sugden, A., et al. 2016, ApJ, 824, 25
Veilleux, S., & Osterbrock, D. E. 1987, ApJS, 63, 295
Watson, L. C., Martini, P., Lisenfeld, U., et al. 2016, MNRAS, 455, 1807
Wen, X.-Q., Wu, H., Zhu, Y.-N., et al. 2014, MNRAS, 438, 97
Wong, O. I., Meurer, G. R., Zheng, Z., et al. 2016, MNRAS, 460, 1106
Wright, E. L., Eisenhardt, P. R. M., Mainzer, A. K., et al. 2010, AJ, 140, 1868
Wu, H., Shao, Z., Mo, H. J., et al. 2005, ApJ, 622, 244
Zhu, Y.-N., Wu, H., Cao, C., & Li, H.-N. 2008, ApJ, 686, 155
Zhu, Y.-N., Wu, H., Li, H.-N., & Cao, C. 2010, RAA (Research in Astronomy and Astrophysics), 10, 329
Zhu, Y., Wu, H., & Jin, J. 2019, ApJ, 874, 79